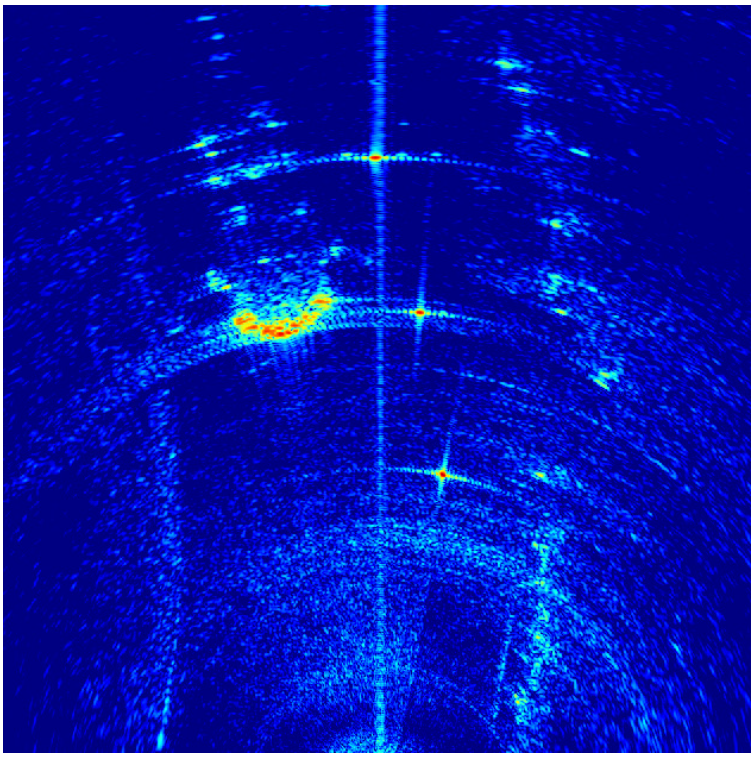

High Resolution Imaging with SAR using Automotive Millimeter Wave Radars

Master's thesis in Communication Engineering

OSKAR LEANDER
VICTOR PETTERSSON

DEPARTMENT OF SPACE, EARTH AND ENVIRONMENT

CHALMERS UNIVERSITY OF TECHNOLOGY
Gothenburg, Sweden 2021
www.chalmers.se

Master's thesis 2021

High Resolution Imaging with SAR using Automotive Millimeter Wave Radars

OSKAR LEANDER
VICTOR PETTERSSON

CHALMERS
UNIVERSITY OF TECHNOLOGY

Department of Space, Earth and Environment
Division of Microwave and Optical Remote Sensing
Radar Remote Sensing
Chalmers University of Technology
Gothenburg, Sweden 2021

High Resolution Imaging with SAR using Automotive Millimeter Wave Radars
OSKAR LEANDER
VICTOR PETTERSSON

© Oskar Leander and Victor Pettersson, 2021.

Supervisors:
Albert Monteith, Department of Space, Earth and Environment
Olof Eriksson, Veoneer

Examiner:
Lars Ulander, Department of Space, Earth and Environment

Master's Thesis 2021
Department of Space, Earth and Environment
Division of Microwave and Optical Remote Sensing
Radar Remote Sensing
Chalmers University of Technology
SE-412 96 Gothenburg
Telephone +46 31 772 1000

Cover: Image of a stationary vehicle produced using synthetic aperture radar imaging algorithms in Matlab.

Typeset in LaTeX
Gothenburg, Sweden 2021

Abstract

Angular resolution is currently one of the main limitations in automotive radars used in advanced driver assistance systems (ADAS). This thesis investigates the possibility of achieving fine-resolution radar images with a commercial, off-the-shelf automotive radar sensor using synthetic aperture radar (SAR). Two imaging algorithms have been investigated and implemented with a Texas Instruments AWR1843 radar system, and the resulting resolution in azimuth has been compared to that of conventional processing methods.

The potential of a side-looking SAR imaging system has been investigated in theory, in simulations and an experimental system was implemented on an actual moving vehicle. Imaging of various automotive scenarios have been performed, and the image quality of the two algorithms, backprojection and Doppler beam sharpening (DBS), has been evaluated. Simulations and measurements show that the resulting system greatly improves azimuth resolution over the conventional multiple-input multiple-output (MIMO) imaging capability of the AWR1843 when in a side-looking mode of operation. The results have helped uncover potential challenges with SAR imaging, such as dynamic scenes and imperfect radar platform motion estimation. The latter problem was overcome using autofocus algorithms.

In conclusion, the devised SAR system shows great promise in delivering fine azimuthal information for improving situational awareness in future ADAS functionality using today's hardware.

Acknowledgements

First and foremost, we would like to thank our supervisor Albert for constantly being available to us during this project and for providing us with invaluable guidance. It is safe to say that this project would have been very difficult without your help. We would also like to thank our supervisor Olof at Veoneer for providing us with technical expertise and experience during our regular meetings. Our project manager Hans at Veoneer deserves a big thank you as well for providing us with materials and for his practical help during our final measurements. The Veoneer crew in Vårgårda deserves gratitude as well for their help with mounting the radar and setting up scenes. Moreover, thank you Lars, our examiner, for directing us towards the DBS algorithm and thank you Jan for helping us with PGA. The rest of the radar remote sensing group deserves a big thank you also for giving us valuable feedback during our half-time presentation. Lastly, we would like to thank all our friends at Chalmers that have supported us during the last five years.

Abbreviations

ADAS	Advanced Driver Assist System
ADC	Analog-to-Digital Converter
BP	Backprojection (algorithm)
CPI	Coherent Processing Interval
DTFT	Discrete Time Fourier Transform
DBS	Doppler Beam Sharpening
FFT	Fast Fourier Transform
FMCW	Frequency Modulated Continuous Wave
IF	Intermediate Frequency
LOS	Line-of-Sight
LP	Low-pass (filter)
MIMO	Multiple-input Multiple-output
PSR	Peak-Sidelobe Ratio
PGA	Phase Gradient Autofocus
PSF	Point Spread Function
RCS	Radar Cross Section
RF	Radio Frequency
RVP	Residual Video Phase
SNR	Signal-to-Noise Ratio
SAR	Synthetic Aperture Radar

Contents

1 Introduction

Like many other aspects of human life, driving is subject to automation with recent developments in technology. New cars are equipped with features such as adaptive cruise control and collision avoidance systems with the aim of increasing the safety of all road users. These type of features are sometimes collectively called advanced driver assistance systems (ADAS) [1]. Situational awareness in ADAS is achieved by perceiving the surrounding environment using sensor technologies, of which radars can make up a large portion [2]. The radar sensor is traditionally associated with military applications not available to the public. But, due to advancements in wireless technology, the radar has gained increasing popularity in the automotive industry and can be found in today's middle-class cars [2]. It is often preferred over other technologies because of its robustness to weather conditions and relatively low cost [2]. In effect, small form-factor and accurate radars are available today operating at millimeter wave frequency bands between 76-81 GHz [3],[1]. A specific class of radars called frequency modulated continuous wave (FMCW) radars are commonly used in automotive applications [3]. The collaborator of this thesis, the company Veoneer, researches and develops leading FMCW radar sensor solutions providing active safety functions in ADAS [4].

Some ADAS functionality require high spatial resolution information from its sensors, and this is seen as a limitation of most automotive radars [2]. Specifically, automotive radar technology needs refinement of its angular resolution in azimuth. Possible technological solutions to this problem include electronically scanned, narrow antenna beams and multiple-input multiple-output (MIMO) antenna configurations [2]. Both mentioned approaches call for multiple transmit and receive antenna channels, which have the disadvantage of adding to hardware cost, size and complexity.

Alternatively, a technique known as synthetic aperture radar (SAR) could be used in some cases. Since the 1950s, SAR processing has allowed radars to be used in imaging applications [5]. The technique aims to retrieve angular information from stationary targets using a moving radar and utilizing the physical phenomenon known as the Doppler shift. Although it has not been clearly demonstrated, it is believed that both dolphins and bats use a similar kind of sonar processing to orientate themselves [6]. The traditional application however, lies in producing high quality 2D images over large swathes of land such as cities, oceans and natural landscapes, using a radar mounted on an aircraft or a spacecraft [7]. What can be considered "large" lies in the eye of the beholder, which in this case means in comparison to the operating wavelength of the radar. In particular, the angular resolution in SAR systems is dependent upon the ratio between the operating wavelength and the observation time [8]. Thus, as millimeter wavelength radar sensors became reality, sufficient azimuth resolution can in principle be obtained using shorter observation times more suitable for automotive applications. Therefore, SAR systems for an automotive use-case has started to become a serious research area generating papers such as [9], [10], [11], [12] and [13].

1.1 Thesis Project Aim

This thesis project aimed to investigate the use of SAR imaging in the automotive use-case. The main research question could be formulated as:

Can useful images of potential traffic scenarios be generated from data recorded with an off-the-shelf automotive radar, using SAR algorithms?

The work first focused on simulating an automotive FMCW radar with MIMO capability. The simulations in combination with theory then aided in the design of an automotive SAR system, complete with two imaging algorithms. An experimental setup was constructed in order to image real scenarios relevant to the automotive use-case. The resulting system was evaluated in its ability to produce high resolution images of various such scenes. The analysis also aimed to identify problematic geometries or objects causing distortions to images, in order to create a survey of main challenges in producing SAR images fit for automotive safety applications.

1.2 Scope

In general, the scenes to be imaged in this project are those seen from a side-looking radar mounted on a moving car. These scenes can include a wide variety of different objects at different ranges, angles and line-of-sight (LOS) clearance relative to the radar. "Objects" or "targets" can refer to other cars, pedestrians and bicycles for example - each with different electromagnetic scattering properties. However, the simulations and radar measurements carried out in this project will focus on rather simplified scenes. The reason is to gain some initial insight into automotive SAR image formation, and to single out the effects of changes by the FMCW radar mode of operation or the operation of the SAR system as a whole. Such simplified scenes will initially consist of an FMCW radar traveling along a straight path observing few targets with well-defined scattering properties such as trihedral corner reflectors for example.

The project uses a specific, commercially available integrated FMCW radar sensor: the Texas Instruments AWR1843BOOST evaluation board mounted on a DCA1000 data capture card as shown in Figure 1. This radar is frequently used in automotive applications with all of its associated constraints on the complexity of the hardware.

The thesis will only include offline processing of data using Matlab, and no extensive investigation of the computational complexity of image formation algorithms will be made. The real-time capabilities of the system and the improvement of such capabilities are therefore not central questions in this project. SAR images will be formed using the backprojection algorithm and Doppler beam sharpening algorithm.

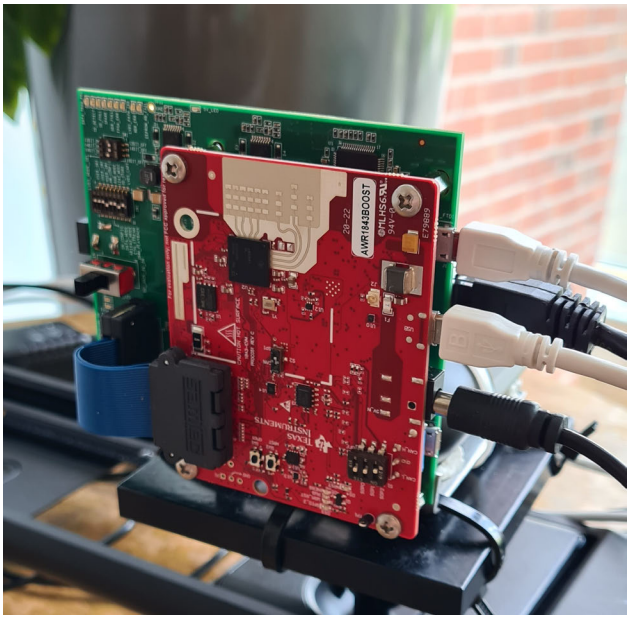

Figure 1: The Texas Intruments AWR1843BOOST radar module used in the project.

1.3 Thesis Outline

Section 2 presents theory uncovered from literature studies part of the thesis work, but also detailed background on implemented algorithms. The section is admittedly rather extensive, but, in the authors' opinions, the extensiveness is motivated because the thesis is, in large, a signal processing task which requires much motivation using mathematical language. Sections 2.1 and 2.2 presents the signal model of FMCW radar data used in this thesis. They lay the foundation of processing steps discussed in following sections, and are important in simulations. Section 2.3 then presents the signal processing concepts typically applied in automotive radars, some of which are useful even in automotive SAR processing, which is presented in Section 2.4. The theory section then concludes with a discussion on phase errors and their effect on SAR images.

In the methodology section, numbered 3, the methods used in order to answer the thesis research question are described. Sections 3.1 and 3.3 cover the acquisition of data from experiments with the AWR1843BOOST radar module and the analysis of such data. Section 3.2 goes into detail on the philosophy behind the simulation tool developed as part of the thesis work.

The results from experiments and simulations are presented, analysed and discussed in Section 4. This leads to the conclusion presented in Section 5. At the very end are appendices listing some mathematical results.

2 Theory & Algorithms

This section aims to first give an in-depth understanding of the Texas Instruments' AWR1843 FMCW radar system, and give a brief description of the processing steps applied in its intended mode of operation. Then, SAR is introduced as a concept and the FMCW radar system is viewed from the SAR imaging perspective. Imaging algorithms used in the thesis work are later presented and motivated. Lastly, an investigation of image degradation due to phase errors is done.

2.1 Introduction to Automotive FMCW Radar

FMCW Radar sensors used in ADAS are typically tasked with estimating the location and velocity of surrounding targets [1],[3]. Specifically, the AWR1843 radar is capable of measuring the range, angle and radial velocity of multiple targets relative to the radar's frame of reference [3]. Together, these three quantities enable the ADAS to perceive other participants or obstacles in the automotive scene and can be used in various ADAS functionalities. Before going into detail about a FMCW radar system model, a brief introduction to range and velocity measurements is made in order to help understand later developments.

A typical automotive radar measurement scenario is depicted in Figure 2. A vehicle with an installed forward-looking FMCW radar wishes to estimate the range and speed of the vehicle ahead. Considering the AWR1843, it is able to achieve this by transmitting a series of linear frequency modulated pulses called chirps via its transmitting antenna. The waveform is reflected off the leading car and the echo is received again by the radar via a separate receiving antenna.

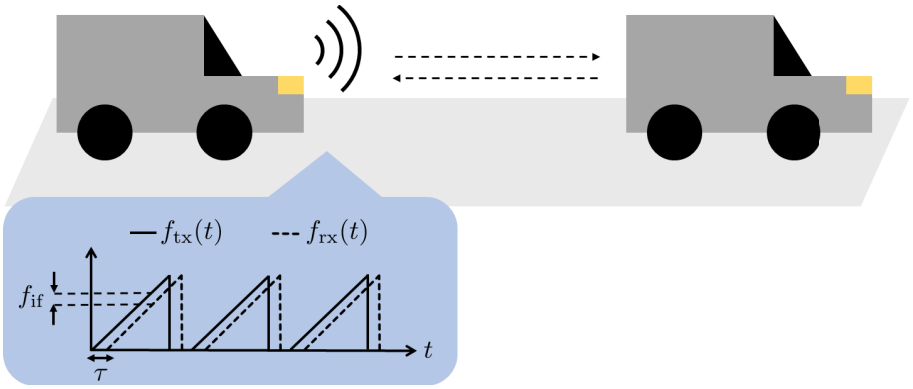

Figure 2: A typical measurement scenario for a FMCW automotive radar. The dashed arrows indicate the propagation path of the waveform and the graph (bottom left) shows instantaneous frequencies $f_{\mathrm{tx}}(t)$, $f_{\mathrm{rx}}(t)$ and f_{if} and τ. These variables are defined below.

Measuring range is equivalent to estimating the time of flight of the radar waveform τ, since:

$$\tau = \frac{2R}{c} \tag{1}$$

where R denotes range and c the speed of light in vacuum. The factor two acknowledges that the waveform travels to and from the leading vehicle. The time of flight will more often be referred to as the delay, since the received echo experiences a time delay of length τ along with some attenuation. This delay is illustrated in the bottom left corner of Figure 2, where the instantaneous frequency of the received signal $f_{\text{rx}}(t)$ is shifted in time compared to the frequency $f_{\text{tx}}(t)$ of the transmit waveform. The radar receiver produces a signal at a frequency equal to the difference $f_{\text{if}} = f_{\text{tx}}(t) - f_{\text{rx}}(t)$ called the intermediate frequency (IF) [3]. And due to the linear modulation of the frequency, characterized by the linear "ramps" of $f_{\text{tx}}(t)$, the IF is proportional to the vehicle-to-vehicle distance according the following expression:

$$f_{\text{if}} = S\tau = S\frac{2R}{c} \tag{2}$$

where S is the slope of the ramps [3],[1]. Thus, by analysis of the IF signal in the frequency domain using Fourier transforms, we can deduct the range of the leading vehicle from the IF using

$$R = \frac{c}{2S} f_{\text{if}} \tag{3}$$

[3],[1]. The range estimation process is sometimes referred to as range compression. Particular to the FMCW waveform, range compression is achieved with Fourier analysis whereas other radar types might use time-domain matched filtering for example [1].

Now imagine that the leading car is traveling faster compared the other, and remember that the FMCW radar transmits and receives a series of multiple chirps. The non-zero, relative radial velocity v_r manifests as a slight shift in phase between consecutive chirps [3], and the shift is characterized by the Doppler frequency:

$$f_D = -\frac{2v_r}{\lambda} \tag{4}$$

where λ is the waveform wavelength. More specifically, v_r is the time derivative of the range, i.e. v_r is positive for an increase in range. The v_r estimate is produced using frequency analysis similar to the range estimate, but this time applied on a chirp-to-chirp basis [3],[1]. From the Doppler frequency the velocity is given by

$$v_r = -\frac{\lambda}{2} f_D. \tag{5}$$

2.2 Automotive FMCW Radar Signal Model

In order to process and simulate FMCW radar data, a detailed mathematical model of the output signal, or the data to be processed, was required. The notation and terminology used in this project was mostly borrowed from Texas Instruments' white paper [3], which specifically covers the basics of the type of sensor used in this work. This white paper went into little detail on the mathematics however, and a project specific model had to be devised.

2.2.1 The FMCW Radar Front End and Waveform

When deriving the signal model, a simple but useful description of the FMCW radar front end has been used for one transmitting and receiving antenna pair. It consists of a waveform generator providing the transmit waveform, the physical channel, a quadrature demodulator and an analog-to-digital converter (ADC) as depicted in Figure 3. Similar descriptions of FMCW radars are found in [3] and [14]. The task of the receiver demodulator is to perform quadrature mixing and filtering on the received echo to produce the IF signal $s_{\text{if}}(t)$, which is later digitized [3],[14].

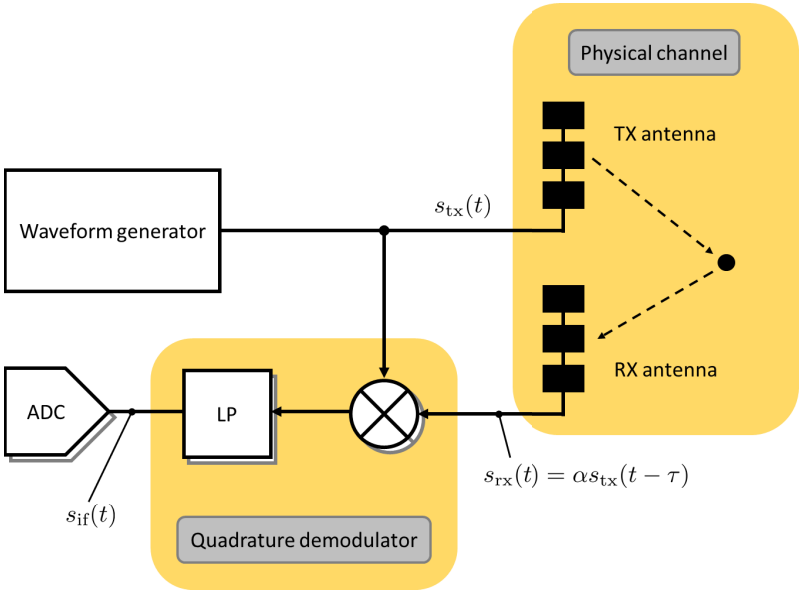

Figure 3: A diagram depicting the FMCW radar front end.

The derivation starts with the transmit waveform produced by the waveform generator, which is a sequence of chirps each followed by a small idle time interval [3]. The time interval between consecutive chirps is called a chirp cycle, and has duration T_c. If a sequence of chirps is transmitted starting at time $t = 0$, then during the first cycle the transmitted signal can be described mathematically by

$$s_{\text{tx}}(t) = \begin{cases} \cos\left(2\pi f_c t + \pi S(t - T/2)^2 + \varphi\right), & 0 \leq t < T \\ 0, & T \leq t < T_c \end{cases} \tag{6}$$

where T is the chirp duration, S is the modulating ramp slope (also called the chirp rate), f_c is the center frequency of the signal and φ is an arbitrary starting phase [14]. The transmit waveform and its instantaneous frequency are illustrated in Figure 4. In the mathematical model, the processed bandwidth is $B = ST$ assuming $ST^2 \gg 1$. The actual transmitted radio frequency (RF) bandwidth is made slightly larger by introducing guard time intervals at both ends of the frequency ramp, during which the received signal is not sampled [15]. This is in order to alleviate hardware effects of the AWR1843 [15], but is not considered in the mathematical model.

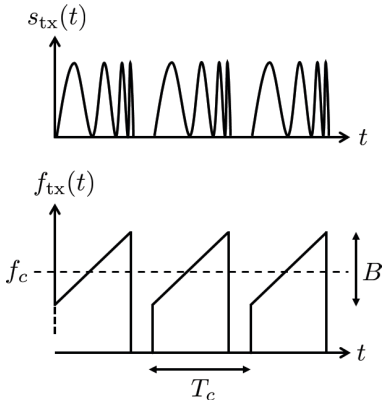

Figure 4: The transmitted waveform of the FMCW radar system (top), and the corresponding frequency $f_{\text{tx}}(t)$ (bottom).

It is necessary to describe a full sequence of M chirps mathematically; such a sequence is called a frame [3]. The transmit signal $s_{\text{tx}}(t)$ is described during the full frame duration, $0 \leq t < MT_c$, by a train of complex pulses modulating a carrier oscillation:

$$s_{\text{tx}}(t) = \mathbf{Re}\left\{ \Big(\sum_{q=0}^{M-1} u(t - qT_c) \Big) e^{\,j(2\pi f_c t + \varphi)} \right\} \tag{7}$$

where

$$u(t) = \begin{cases} e^{\,j\pi S(t - T/2)^2}, & 0 \leq t < T \\ 0, & \text{otherwise} \end{cases} \tag{8}$$

is the complex envelope which describes the frequency modulation similar to descriptions found in [1] and [16]. Evaluating (7) for $0 \leq t < T_c$, we again get the expression in (6) for $s_{\text{tx}}(t)$ during the first cycle. We can ignore the sum by considering only the m:th chirp cycle:

$$s_{\text{tx}}(t) = \mathbf{Re}\left\{ u(\hat{t}) e^{\,j(2\pi f_c t + \varphi)} \right\}, \quad \text{for } mT_c \leq t < (m+1)T_c \tag{9}$$

as all terms $u(t - qT_c) = 0$ for all $q \neq m$. Importantly,

$$\hat{t} = t - mT_c \tag{10}$$

is a time variable which starts anew at the beginning of each chirp as described in [16], where it is referred to as fast time. The index $m = 0, 1, 2, \ldots, M-1$ is called the chirp index or the chirp number.

Using the model for the transmit waveform in (9), we can derive the received IF signal observed before the ADC. As depicted in Figure 3, the received echo from one target $s_{\text{rx}}(t)$ is an attenuated and time delayed version of the transmitted waveform, where α denotes an attenuation constant and τ denotes the time-of-flight delay proportional to the target range. The quadrature mixer splits the received echo in two, and mixes one channel with the transmitted waveform and the other with a replica but shifted $\pi/2$ (or 90°) in phase in order to create in-phase and quadrature-phase channels (I and Q). Such a mixer is described in [17]. The mixing procedure is modeled as a multiplication and, by treating the I and Q channels simultaneously in the form of a complex number, the product can be written as

$$\alpha s_{\text{tx}}(t - \tau) u(\hat{t}) e^{\,j(2\pi f_c t + \varphi)} \tag{11}$$

where $s_{\text{tx}}(t-\tau)$ is as described in (9), but shifted in time by an amount τ. The low pass (LP) filter then acts on this product to finally produce the IF signal observed at the quadrature demodulator output. Its expression is found by removing the high frequency terms revealed when computing (11), and becomes

$$s_{\text{if}}(t) = \begin{cases} \alpha \exp j\left(2\pi S\tau(\hat{t} - T/2) + 2\pi f_c\tau - \pi S\tau^2\right)/2, & mT_c \leq t < mT_c + T \\ 0, & mT_c + T \leq t < (m+1)T_c \end{cases} \tag{12}$$

assuming that $\tau \ll T$. This assumption is valid in automotive scenarios, as $\tau \sim 0.1\,\mu\text{s}$ even for long range applications, while $T \sim 10\,\mu\text{s}$ [15]. The expression for the IF signal in (12) is important and is recurrent throughout this thesis as it is fundamental in the majority of the applied processing steps.

2.2.2 General Model of Digitized FMCW Radar Data

The IF signal is sampled by the ADC with a sampling rate $f_s = 1/T_s$ at instances

$$t = nT_s + mT_c \tag{13}$$

where n is the discrete equivalent of the $\hat{t}$ variable. It is defined for $n = 0, 1, 2, \ldots, N-1$, where N is the number of samples gathered during the active time of each chirp cycle [3]. This expression of time is a reordering of (10), with the substitution $\hat{t} = nT_s$. The discrete time variables n and m can be thought of as two different dimensions in a 2D matrix as described in [17] called fast time and slow time respectively. By holding the chirp index m fixed, and alternating n we observe samples within only one chirp in the fast-time dimension. By instead alternating m and holding n fixed, we observe the signal in slow time on a chirp-to-chirp basis [17]. These two concepts are important in the processing of the FMCW radar data, especially for SAR, and will be mentioned frequently throughout this text.

By inserting $\hat{t} = nT_s$ into the expression in (12), while at the same time emphasizing the time-dependence of the delay by writing $\tau = \tau_{n,m}$, we can formulate the general model for the observed data matrix:

$$s_{\text{if}}(n,m) = \frac{\alpha}{2} \exp j\left(2\pi S\tau_{n,m}(nT_s - T/2) + 2\pi f_c\tau_{n,m} - \pi S\tau_{n,m}^2\right). \tag{14}$$

The m-dependence in (14) is embedded entirely in $\tau_{n,m}$, which is the delay τ evaluated at discrete time instances (n,m). Detailed models of the time-variability of $\tau_{n,m}$ are of great importance in automotive radar processing and SAR, and will be discussed in more detail in later sections. It is easy to realize that τ can be time-dependent in dynamic radar-target scenarios when it is written as a function of target range:

$$\tau(t) = \frac{2R(t)}{c} \tag{15}$$

where the range $R(t)$ is the relative distance between the radar and target. Any relative movement between the two will vary $R(t)$ over time. The expression in (15) assumes that the time derivative of the range is much less than the speed of light.

For MIMO radars, multiple channels are made up of multiple transmitting and receiving antenna pairs as will be explored later. A complete description of AWR1843 data is thus

a set of 2D matrices described by (14), one for each channel, creating a 3D data matrix or "cube" as illustrated in Figure 5.

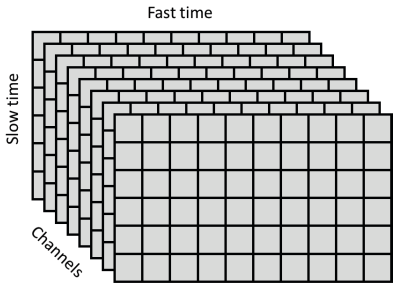

Figure 5: Useful representation of automotive FMCW radar data as a 3D matrix or cube.

2.2.3 Identifying the Phase Terms

Observing the IF signal in (12), we see that the phase, the argument of the complex exponential, consists of three terms. It is helpful to distinguish between these as they play different roles in the processing tasks carried out in this work.

1. The first term, $2\pi S\tau(\hat{t} - T/2)$, is referred to as the IF term, since it contains the IF observed in fast time $f_{\text{if}} = S\tau$.
2. We call the second term, $2\pi f_c \tau$, the Doppler term. We will later see that it conveys Doppler information.
3. Lastly, the third term, $-\pi S\tau^2$, is the residual video phase (RVP) described in [16]. This term is sometimes of concern in imaging applications using linearly frequency modulated waveforms with demodulation.

2.3 Processing in Automotive FMCW Radars

Here is a theoretical treatment of common automotive FMCW radar processing, using the developed signal model. Mathematical relations presented in Section 2.1 will be derived in addition to other important figures of merit in both automotive radar and SAR. The AWR1843 is capable of imaging using MIMO antenna arrays. This technique is also presented, as such processing will be used as a benchmark when performing SAR.

2.3.1 Estimating Range and Velocity from the Target Response

Assume that a stationary radar observes a dynamic target with a constant relative radial velocity v_r at mean range $\bar{R}$. We can describe the range over time as

$$R(t) = \bar{R} + v_r(t - T_{\text{frame}}/2) \tag{16}$$

where T_{frame} is the duration of one frame (the transmission of M chirps). The signal model described by (12) can be approximated by

$$s_{\text{if}}(\hat{t}, m) = \frac{\alpha}{2} \exp j \left(2\pi S \bar{\tau} (\hat{t} - T/2) + 2\pi f_c \tau_m \right) \tag{17}$$

where delay is given by

$$\bar{\tau} = \frac{2\bar{R}}{c} \tag{18}$$

in the first term and

$$\tau_m = \frac{2\left(\bar{R} + v_r(mT_c - T_{\text{frame}}/2)\right)}{c} \tag{19}$$

in the second. The third term (the RVP) is practically constant during the frame and is approximated as an arbitrary constant value of zero. The coarse approximation of τ in the first term into a constant $\bar{\tau}$ disregards the fact that the radar sees a spectrum of ranges around $\bar{R}$ over the frame time. We here assume that the extent of this spectrum is negligible, meaning that it is smaller than a resolution cell. This approximation is done in favor of the analytical development and implementation, and the assumption is not necessarily true all the time. For the Doppler term, the delay τ_m is said to only vary chirp-to-chirp. This approximation is similar to the "start-stop" approximation commonly applied in SAR, and its validity for FMCW systems is discussed in [18].

By inserting (18) and (19) into (17) we eventually get

$$s_{\text{if}}(n, m) = \frac{\alpha}{2} \exp j \left(2\pi S \left(\frac{2\bar{R}}{c} \right) n T_s + 2\pi f_c \left(\frac{2v_r}{c} \right) m T_c + \varphi' \right) \tag{20}$$

after digitizing the IF signal. The φ'-variable is a constant phase term and is not interesting for estimating range or velocity. Note that $s_{\text{if}}(n, m)$ has two linear terms in n and m respectively. Speaking in terms of discrete time signals, these linear terms have rates equal to normalized angular frequencies:

$$\Omega_{\text{fast}} = 2\pi S \frac{2\bar{R}}{c} T_s \tag{21}$$

$$\Omega_{\text{slow}} = 2\pi f_c \frac{2v_r}{c} T_c \tag{22}$$

where Ω_{fast} and Ω_{slow} are observed in fast and slow time respectively. These frequencies, along with their encoded information, can be estimated using digital frequency analysis with fast Fourier transforms (FFTs) [3],[16],[1]. The estimation process can be analyzed analytically using the continuous counterpart, the discrete time Fourier transform (DTFT). The 2D-DTFT of both n and m dimensions is defined as

$$S(\Omega_R, \Omega_v) = \text{DTFT}_{n,m}\{ s_{\text{if}}(n, m) \} = \sum_m \sum_n s_{\text{if}}(n, m) e^{-j\Omega_R n} e^{-j\Omega_v m} \tag{23}$$

where Ω_R and Ω_v are normalized angular frequency variables corresponding to the fast- and slow-time dimensions respectively. The DTFT is used to form the 2D periodogram, which measures the signal energy at each pair of frequencies (Ω_R, Ω_v):

$$\begin{aligned} P(\Omega_R, \Omega_v) &= \frac{|S(\Omega_R, \Omega_v)|^2}{MN} \\ &= \frac{\alpha^2}{4MN} \left| \frac{\sin\big(N(\Omega_R - \Omega_{\text{fast}})/2\big)}{\sin\big((\Omega_R - \Omega_{\text{fast}})/2\big)} \cdot \frac{\sin\big(M(\Omega_v - \Omega_{\text{slow}})/2\big)}{\sin\big((\Omega_v - \Omega_{\text{slow}})/2\big)} \right|^2 \end{aligned} \tag{24}$$

where the derivation of the last expression is presented in Appendix A. $P(\Omega_R, \Omega_v)$ can be thought of as a surface, or an image, with a spike at $(\Omega_R, \Omega_v) = (\Omega_{\text{fast}}, \Omega_{\text{slow}})$ indicating the presence of the one target. For multiple targets, the IF signal is a superposition of multiple components similar to the right side of (17), resulting in multiple spikes.

The estimated range and velocity of the target are found by scaling the coordinate axes of the periodogram to create a (R, v_r)-surface, which is sometimes called a range-velocity-map (RV-map) in automotive radar applications. From (21) and (22) we get the mapping

$$R = \frac{c}{2S}\frac{\Omega_R}{2\pi T_s} = \frac{c}{2S} f_{\text{if}} \tag{25}$$

$$v_r = \frac{c}{2f_c}\frac{\Omega_v}{2\pi T_c} = -\frac{\lambda}{2} f_D \tag{26}$$

where the normalized angular frequencies are now replaced by the physical frequencies. The bar over R is dropped for consistency. These are the relations presented in Section 2.1, now derived from the signal model.

The theoretical response from a target with $(R, v_r) = (12\,\text{m}, 4\,\text{m/s})$ observed by a radar is shown in Figure 6. It is displayed in decibels or dB relative its maximum value according to

$$P(R, v_r)_{\text{dBmax}} = 10\log_{10}\left(P(R, v_r)/\max_{R, v_r} P(R, v_r)\right). \tag{27}$$

A distinct spike is seen at the correct target coordinates. The main spike, called the mainlobe, is not infinitely narrow and surrounding the mainlobe are sidelobes. The nearest sidelobes can be of significant intensity which can obstruct the view of another, closely located target in (R, v_r)-space.

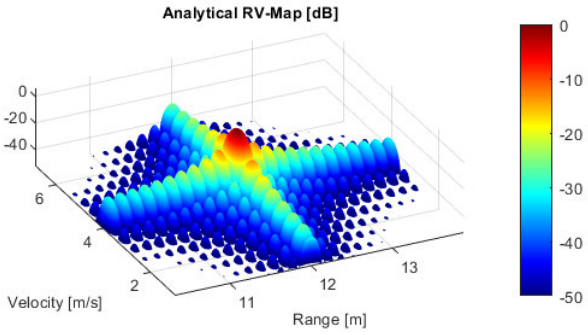

Figure 6: Target response shown in a RV-map calculated using the analytical expression in (24).

It is possible to reduce the sidelobe intensity using weighting functions on time-domian data before applying the Fourier transform. Such functions, sometimes called windows, involves a trade-off in the sidelobe reduction and broadening of the response mainlobe however [19]. Processing tasks in this thesis work sometimes utilize the Hann window mentioned in [19].

2.3.2 Range and Velocity Resolution

Using the results developed in the last section, we can find the resolution in R and v_r. These two quantities determine how far separated two scatterers must be in (R, v_r)-space for them to be perceived correctly [3]. If they are too close, their respective responses' mainlobes will be superposed and perceived together as one target.

We define the resolution values δ_R and δ_v for range and velocity as the peak-to-first-null widths of the target response mainlobes dictated by (24) in respective dimension. They can be shown to equal

$$\delta_R = \frac{c}{2B} \tag{28}$$

$$\delta_v = \frac{\lambda}{2MT_c} \tag{29}$$

by analysing respective cuts in range and velocity of (24). These are also the same resolution results presented in [15]. It is important to note that the bandwidth in (28) is the processed bandwidth $B = ST = SNT_s$ mentioned in Section 2.2.1.

2.3.3 Velocity Ambiguity and Maximum Range

Here are presented two quantities that determine the extent of the (R, v_r)-surface observed by the automotive radar system. These quantities also turn out to be fundamental when determining the area of the imaged scene in the later proposed automotive SAR system.

Due to a well known result in Fourier theory, Doppler measurements are ambiguous with other frequencies larger in magnitude $|f_D| > 1/(2T_c)$. This motivates the formulation of a maximum unambiguous velocity

$$v_{\max} = \frac{\lambda}{2} \cdot \frac{1}{2T_c} = \frac{\lambda}{4T_c} \tag{30}$$

commonly mentioned in radar Doppler processing. Also, specifically to the FMCW waveform, the observed range is limited by the maximum observable IF, which is (almost) the sampling frequency f_s [15]. This give the maximum range

$$R_{\max} = \frac{c}{2S} f_s. \tag{31}$$

Any reflections from targets at longer ranges are filtered out by the LP-filter (anti-alias).

2.3.4 Measuring Angle with MIMO Radars

The AWR1843BOOST radar applies a 2×4 MIMO antenna configuration in azimuth, meaning that it has two transmitter and four receiver antennas as illustrated in the left part of Figure 7. As described in [20], the carefully spaced transmitters can take turns in transmitting each chirp of a frame (time-division multiplexed MIMO), which eventually

reach the receivers after being scattered off a target. This means that for every two consecutive chirps the radar experiences eight unique propagation paths for the same scatterer. This information can be used to form eight equally spaced virtual monostatic antennas [15], which are illustrated to the right in Figure 7. Each channel is shifted in phase relative to its neighbours by an amount depending on the angle of arrival θ_a of the received waveform [3]. Using a plane wave approximation, this change in phase over channels is constant, meaning that phase progresses linearly on a channel-to-channel basis [3]. The right part of Figure 7 illustrates the more conceptual view of the MIMO radar used in theory, as opposed to the factual (left).

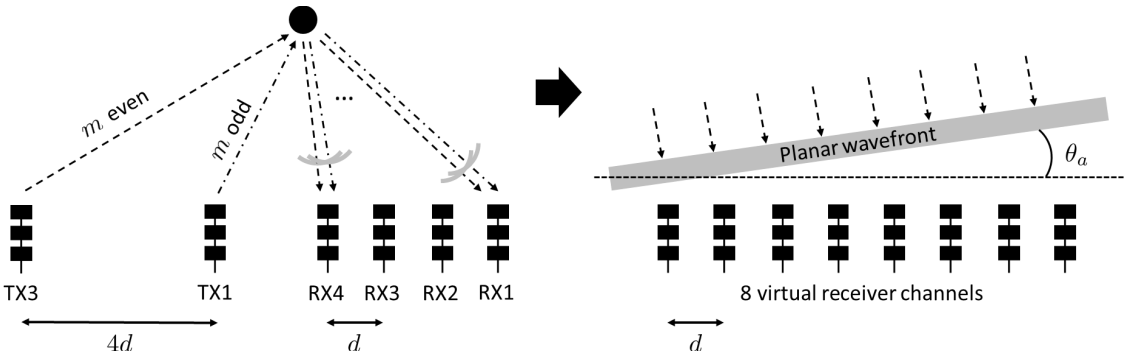

Figure 7: Factual (left) and conceptual (right) view of the MIMO radar. Dashed and dashed/dotted arrows indicate waveform propagation paths.

In effect, a range-angle map can be constructed from a 2D matrix $s_{\text{if}}^{(\ell)}(n)$, where the superscript $\ell = 0, 1, 2, \ldots, L-1$ indicates the virtual channel number out of L in total. Range and angle responses are compressed in both dimensions again via a 2D FFT in n and ℓ, since the linear phase progression over channels can be thought of as a constant spatial frequency. The coordinate transform for the angular dimension is

$$\theta_a = \arcsin\left(\frac{\lambda}{2\pi d}\Omega_{\theta_a}\right) \tag{32}$$

where d is the MIMO element spacing and Ω_{θ_a} is the observed constant phase shift or spatial frequency [3]. Similar to RV-maps discussed in previous sections, a range-angle surface is created using the compressed data with scaling of the axes. Sometimes we refer to such a surface as a range-angle-map (RA-map).

The angular resolution is

$$\delta_{\theta_a} = \frac{\lambda}{Ld\cos\theta_a} \tag{33}$$

and is dependent on the angle θ_a itself due to the non-linearity of the arcsin-function [15]. For the AWR1843BOOST, we have $L = 8$ and $d = \lambda/2$ yielding

$$\delta_{\theta_a} = \frac{\lambda}{8 \cdot \lambda/2} \cdot \frac{180^\circ}{\pi} \approx 14^\circ \tag{34}$$

at best for $\theta_a = 0^\circ$. This is in the direction normal to the array/aperture which will be referred to as the array "boresight direction" or just "boresight" in this thesis, as commonly done in radar literature.

2.3.5 Implementation of Algorithms

To finalize the discussion on automotive radar processing, we present schematic illustrations of algorithms based on the theory presented. They are shown operating on different cuts of the data cube in Figure 8. Note that the MIMO processing results in a spatial image $I(x, y)$, after converting the RA-map to Cartesian coordinates. The resulting cross-range resolution in Cartesian space becomes

$$\delta_{\text{cr}} = R\delta_{\theta_a} \tag{35}$$

for spatial images produced with MIMO processing.

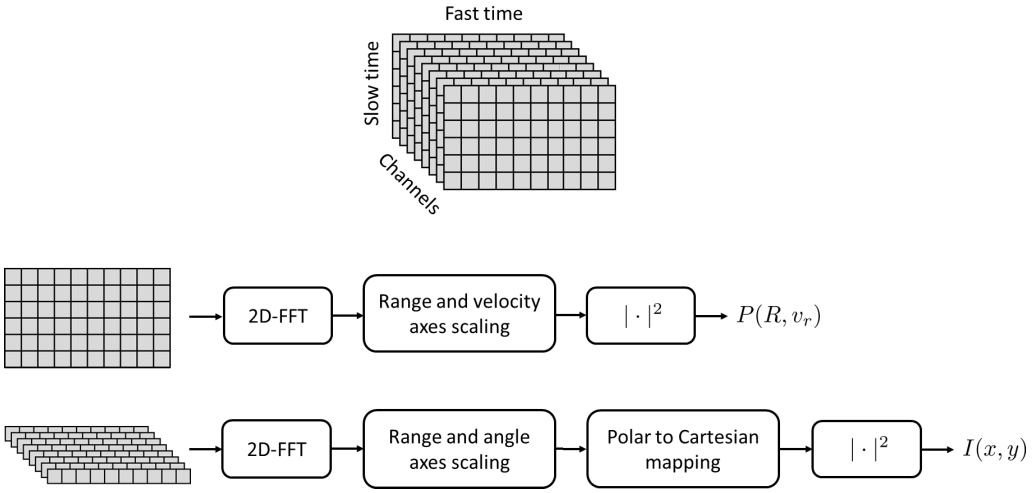

Figure 8: A chart illustrating the processing steps when forming RV- and RA-maps, $P(R, v_r)$ and $I(x, y)$, respectively, from cuts of the raw IF signal data in the data cube.

2.4 Automotive SAR

Depending on the geometric assumptions of the particular signal model being used, the phase terms in the digitized model shown in (14) can be thought of as being associated to different physical quantities. For example, we have seen that target range and velocity can be estimated by observing the IF and Doppler term respectively for the automotive FMCW radar system in its normal mode of operation. In this section, we investigate the IF signal when the radar is used in a proposed side-looking SAR mode of operation and develop processing steps in order to reveal range and angular information from only one channel as opposed to multi-channel MIMO processing.

This thesis work defines "automotive SAR" as the action of producing spatial images by means of processing the fast- and slow-time dimensions of a single channel of a side-looking automotive radar as it is moving with a certain constant velocity. As opposed to traditional airborne SAR, imaged objects are approximately located in the same plane as the radar, which is looking straight out along a line parallel with the ground. A top view of the geometry is displayed in Figure 9, where the gray box represents a car with an installed, side-looking radar. The grid represents constant radial range- and azimuth

angle-contours, and the intersection of such contours are represented in polar coordinates by (R, θ) referenced to the radar. The angle θ is always relative to the velocity vector of the radar platform.

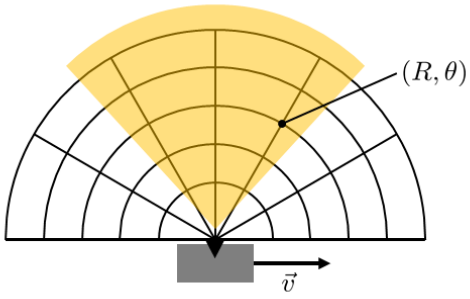

Figure 9: Automotive SAR imaging geometry together with constant range and azimuth angle contours.

2.4.1 Synthetic Aperture

In SAR, it is assumed that the targets are stationary and the radar moves while it transmits and receives chirps. The simplest case is when the radar moves with a constant velocity along a straight path that coincides with a coordinate axis as shown in Figure 10, and a single target is present. Since the chirps are received in discrete points in time, the acquired data will consist of echoes collected from multiple antenna positions, hence the name synthetic aperture radar. The principle is illustrated in Figure 10.

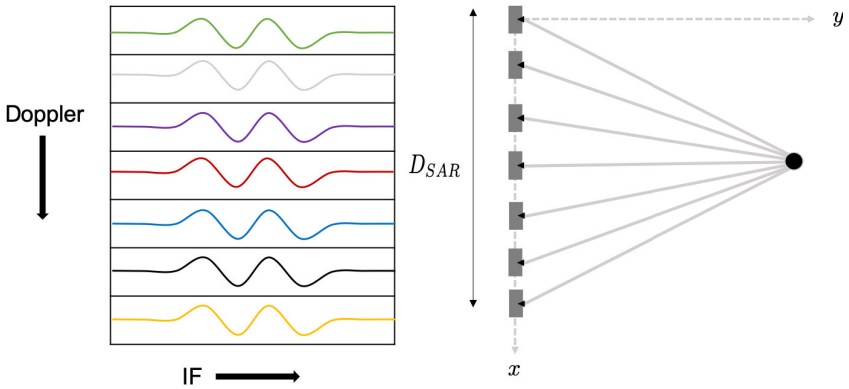

Figure 10: Data collection geometry for automotive SAR.

In Section 2.4.4, we will show that the required platform motion to achieve fine azimuth resolution is relatively short, meaning that for most practical situations, Figure 10 is not drawn up to scale. The length of the synthetic aperture is given by

$$D_{\text{SAR}} = v_x M T_c = v_x \text{CPI} \tag{36}$$

where CPI is the coherent processing interval of the system and refers to the total acquisition time for one set of SAR data.

2.4.2 Image Formation using Doppler Beam Sharpening

An algorithm for angular refinement in azimuth for automotive radars is presented in [11], called Doppler beam sharpening (DBS), and is applied in this thesis work. The algorithm is inspired by an early SAR-technique that dates back to the year 1951, when it was first put forth by Carl Wiley, and is based on a Doppler shift-argument [7]. The processing involves frequency analysis using FFTs, as demonstrated in [11], followed by Doppler to azimuthal angle conversion and a polar to Cartesian coordinate mapping. The following text goes into detail on the algorithm, in order to understand its strengths and limitations.

Referring again to Figure 9, imagine a stationary target is located at the coordinates (R, θ). As the radar travels with velocity $\vec{v} = v_x\hat{x}$ past the target, the relative speed experienced by the radar due to the target is the projection $v_r = -v_x \cos\theta$ onto the radar-to-target vector [8]. The observed Doppler shift is

$$f_D = -\frac{2}{\lambda} \cdot (-v_x \cos\theta) = \frac{2v_x}{\lambda} \cos\theta \tag{37}$$

and encodes angular information about the target which we desire to extract. Thus, we are once again tasked with estimating range and velocity/Doppler from the IF signal modeled as

$$s_{\text{if}}(n, m) \propto \exp j \left(2\pi S \left(\frac{2\bar{R}}{c} \right) nT_s - 2\pi f_c \left(\frac{2v_x \cos\theta}{c} \right) mT_c \right) \tag{38}$$

in accordance with (20) presented in Section 2.3.1 where v_r is now replaced by $-v_x \cos\theta$. This data is again in the form suitable for compression using FFTs in both fast- and slow-time dimensions, as also described in Section 2.3.1. A range-Doppler surface is created in a similar fashion to a range-velocity surface, and can be converted to range-angle by the following relation

$$\theta = \arccos\left(\frac{\lambda f_D}{2v_x} \right) \tag{39}$$

which is a rearrangement of (37) and is also demonstrated in [11]. Cartesian coordinates are found using the transform:

$$x = R\cos\theta \tag{40}$$

$$y = R\sin\theta. \tag{41}$$

The resulting target response in (x, y) is known as the point spread function of the imaging algorithm, and determines the achieved resolution. As it is produced in similar ways to RV-maps discussed in Section 2.3.1, the resulting resolution in range is also δ_R described by (28). The angular resolution, or the resolution in cross range after polar to Cartesian mapping, is discussed later in Section 2.4.4.

A schematic view of the actual implementation in this thesis is shown in Figure 11, where $I(x, y)$ is the resulting power image. The interpolation step of the Doppler dimension is required for equally spaced angular samples.

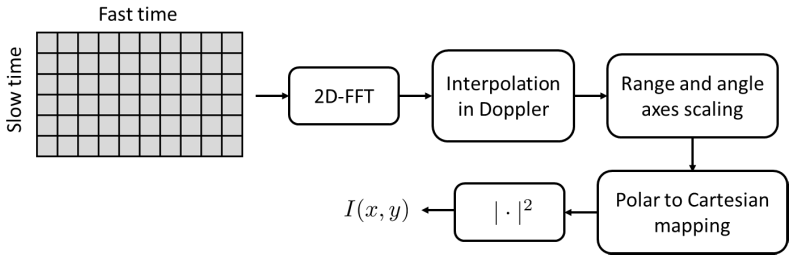

Figure 11: Schematic view of the implemented DBS algorithm.

Limitations of the DBS algorithm are now discussed to conclude this section:

- As the radar moves along the synthetic aperture, the relative distances of targets change. If this change is significant, it is known as range migration in SAR literature [8]. DBS assumes no range migration, as the range $\bar{R}$ is again approximated as a constant in the IF term of (38). The algorithm is hence expected to be limited in its ability to produce high resolution images when the approximation does not hold. Range migration is also mentioned briefly in [11], but referred to as range walk.
- The Doppler term is linear in m, as the relative speed $-v_x \cos\theta$ is assumed constant. This is also an approximation, since the relative angle is a function of the radar-to-target vector, $\vec{R}(t)$, which clearly changes as the radar moves over the aperture. It is realized that the approximation is rather good for ranges $R \gg D_{\text{SAR}}$, but is also seen as a limiting factor of the algorithm. This phenomenon is mentioned as Doppler walk in [11].

2.4.3 Image Formation using Backprojection

Another method for radar imaging is known as backprojection, sometimes referred to as BP, and the motivation why its included in this text is that it relies on fewer assumptions than DBS. A mathematical derivation of backprojection for pulsed radar systems can be found in [21]. For FMCW waveforms the model needs a few adjustments as described by [9], [13] and [18]. The basic principle behind the algorithm, however, is the same and builds upon tracking the phase evolution of the Doppler delay term from each possible target position in a predefined region of interest. The region of interest can have any arbitrary shape but in this text we will assume all scenes to be square where one edge coincides with the ideal radar trajectory. The considered geometry is depicted in Figure 12 and all possible target positions will be referred to as pixels.

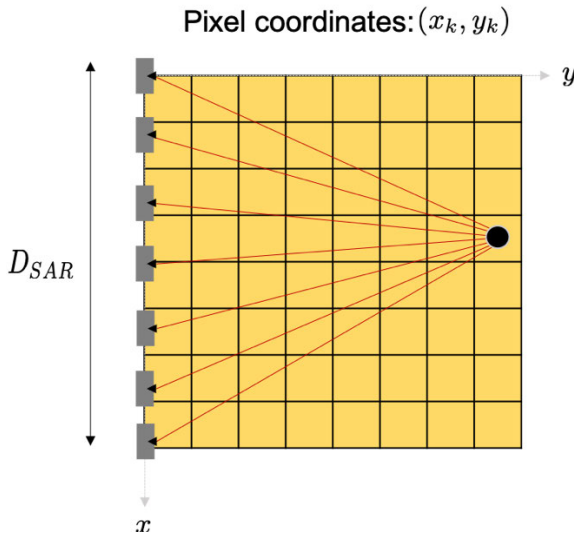

Figure 12: Considered geometry for SAR image formation using backprojection.

The version of backprojection that is presented in this text will make use of what in SAR literature is known as a start-stop approximation [18], meaning that the radar and the target are assumed to remain stationary during transmission and reception of a chirp. In mathematical terms this means that the delay term is independent from the fast-time variable, which can be expressed as

$$\tau_m = \left.\frac{2R(t)}{c}\right|_{t=mT_c}. \tag{42}$$

And the digitized signal model used in backprojection can thus be written as

$$s_{\text{if}}(n,m) = \frac{\alpha}{2}\exp j\left(2\pi S\tau_m(nT_s - T/2) + 2\pi f_c\tau_m - \pi S\tau_m^2\right). \tag{43}$$

As the automotive SAR system applies FMCW waveforms, backprojection operates on the complex, range compressed IF-signal:

$$S(\Omega_R, m) = \frac{\alpha}{2}e^{-j\Omega_R(N-1)/2}\cdot \text{Dir}_N(\Omega_R - \Omega_{\text{fast}})\cdot e^{j(2\pi f_c\tau_m - \pi ST_s\tau_m - \pi S\tau_m^2)} \tag{44}$$

where $\text{Dir}_N(\Omega_R - \Omega_{\text{fast}})$ is a shifted Dirichlet kernel discussed in Appendix A. The derivation of the entire expression can be found in Appendix B.

To connect the range compressed signal with the geometrical model in Figure 12, we consider the return signal from a target at pixel k with coordinates (x_k, y_k). Geometrically we can say that the one-way distance between the target and the receiving antenna at a particular slow-time index is

$$R_{m,k} = \sqrt{y_k^2 + (x_k - a_m)^2} \tag{45}$$

where a_m is the x-coordinate of the antenna. The corresponding delay and normalized angular fast-time frequency are expressed as:

$$\tau_{m,k} = \frac{2R_{m,k}}{c} \tag{46}$$

$$\Omega_{m,k} = \frac{4\pi S T_s R_{m,k}}{c}. \tag{47}$$

The rest of the mathematical details of backprojection can be found in Appendix B and here we present the result in the form of a block diagram instead. As is shown in Figure 13, the range compressed signals are filtered in the frequency domain and then linearly interpolated to be well defined at the quantities that are related to the pixel coordinates at hand. The Doppler phase term can then be removed so that coherent summation can be made in slow time. The remaining quantity is then a measure of the reflectively at a particular pixel coordinate and we use the absolute squared magnitude as the colour dimension in our image. The final expression is:

$$I_k = \frac{\alpha^2}{4} \left| \sum_{m=0}^{M-1} \mathrm{Dir}_N(\Omega_{m,k} - \Omega_{\text{fast}}) \right|^2. \tag{48}$$

The process is repeated for each pixel to form an intensity image.

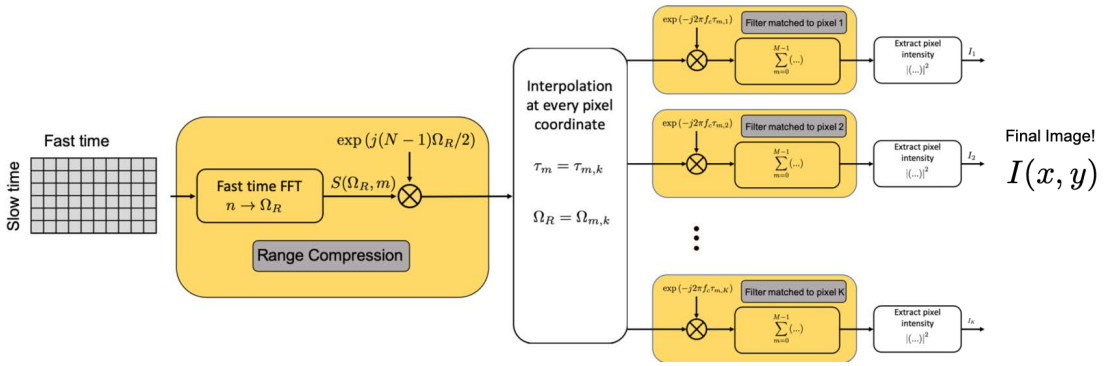

Figure 13: A block diagram that illustrates how the backprojection algorithm is implemented in this project. The mathematical details can be found in Appendix B.

2.4.4 SAR Azimuth and Cross-Range Resolution

In general, the resolution (peak-to-first-null mainlobe width) of a SAR system in the cross-range dimension is

$$\delta_{\text{cr}} = \frac{\lambda}{2\Delta\theta} \tag{49}$$

where $\Delta\theta$ is the integration angle [8]. Typically for airborne side-looking radars, the integration angle is equal to the beamwidth of the antenna due to long synthetic apertures [8]. But, more interesting for automotive applications are shorter apertures, requiring shorter collection times and resulting in relatively small integration angles less than the antenna beamwidth. This section investigates the cross range resolution achieved in such geometries.

First, consider a point target at boresight ($\theta = 90°$) observed with synthetic aperture length D_{SAR}. For ranges $R \gg D_{\mathrm{SAR}}$, the integration angle is approximately $\Delta\theta \approx D_{\mathrm{SAR}}/R$, which yields

$$\delta_{\mathrm{cr}} = \frac{R\lambda}{2D_{\mathrm{SAR}}} \tag{50}$$

and is the best achievable resolution of the automotive SAR system. Notice that it is coarser for longer ranges.

More insight is achieved using the angle-Doppler relation in (39) for DBS. Written in terms of velocity we have

$$\theta = \arccos\left(\frac{-v_r}{v_x}\right) \tag{51}$$

and we define the angular resolution in azimuth δ_θ as the result from a small perturbation in velocity given by the velocity resolution δ_v. A first-order Taylor expansion of (51) yields

$$\delta_\theta = \left|\frac{d\theta}{dv_r}\right| \delta_v = \frac{1}{v_x \sin\theta} \cdot \frac{\lambda}{2MT_c} = \frac{\lambda}{2D_{\mathrm{SAR}} \sin\theta} \tag{52}$$

for angles $\theta \in [0°, 180°]$ and using $v_x MT_c = D_{\mathrm{SAR}}$. Thus, the cross range resolution becomes

$$\delta_{\mathrm{cr}} = R\delta_\theta = \frac{R\lambda}{2D_{\mathrm{SAR}} \sin\theta} \tag{53}$$

which is consistent with the former expression at boresight. It is now evident that the resolution gets coarser with deviations in θ from 90° (boresight). Geometrically, (53) can be interpreted as the synthetic aperture being projected onto a plane normal to the aperture center-to-target vector. This reduces the effective aperture by a factor $\sin\theta$. In comparison to the angular resolution in azimuth for MIMO imaging in (33), we see that the SAR resolution is made finer by a factor two for the same array or aperture length (when $Ld = D_{\mathrm{SAR}}$).

2.5 Phase Errors in Imaging

The quality of SAR images can be severely degraded by phase errors. Common effects include geometric distortion, spurious targets, reduction in resolution and a loss in signal to noise ratio (SNR) [22]. The main causes of those errors are uncompensated motion errors from the scene of interest and errors that arise from the approximations made in the image formation algorithm. Phase errors in SAR images can often be characterized as either being spatially invariant or variant, meaning that all scatters in an image are affected equally or not by the particular phase error at hand. Later in this section an algorithm will be presented that deals with spatially invariant phase errors.

2.5.1 Phase Error due to Vibrations

SAR image formation requires precise knowledge of the antenna phase center positions during data acquisition. If that information is unavailable, or for any other reason remains uncompensated, phase errors will arise after image formation. To develop simple analytical

models of those errors we will use [22], where it is stated that the resulting phase error ϕ_e from an uncompensated LOS deviation of size R_e, is given by

$$\phi_e = \frac{4\pi R_e}{\lambda_c}. \tag{54}$$

Due to the vibrations experienced by a vehicle on the road, a motion error of particular interest is sinusoidal cross-track motion errors. The mathematical expression for a position error of this kind is described by

$$R_e = A_e \sin\left(2\pi f_e m T_c\right) \tag{55}$$

where A_e and f_e is the amplitude and frequency of the vibration. The corresponding phase error is given by

$$\phi_e = \phi_0 \sin\left(2\pi f_e m T_c\right) \tag{56}$$

where $\phi_0 = 4\pi A_e/\lambda_c$. Following the derivations made in [22], where it is assumed that ϕ_0 is small, one can approximate $\exp j(\phi_e)$ according to

$$\exp j(\phi_e) \approx 1 + \frac{\phi_0}{2}\bigg(\exp j(2\pi f_e m T_c) - \exp j(-2\pi f_e m T_c)\bigg). \tag{57}$$

To relate this phase error to effects that can be seen in an image, we use the simplified assumptions of DBS were azimuth compression was achieved with a Fourier transform in the slow-time domain. Since the phase error function also is dependant upon slow time, the multiplication in time domain will turn up as a frequency domain convolution between the azimuth compressed SAR signal and the Fourier transform of the phase error function, which in this case is simply three Dirac delta spikes with one in the center and two symmetric copies at frequencies given by $\pm f_e$. Thus, in an ideal scenario with one target at boresight, the azimuth cut of the SAR signal with a sinusoidal phase error is a Dirichlet kernel at zero Doppler with two paired echos at the vibration frequency $\pm f_e$. The effect is shown in Figure 14 and the connection between Doppler frequencies and angles in a SAR image follows from (39).

A key metric for sinusoidal phase error is the peak sidelobe ratio (PSR) given by

$$\mathrm{PSR} = 10\log_{10}\left(\frac{\phi_0^2}{4}\right) = 20\log_{10}\left(\frac{2\pi A_e}{\lambda_c}\right). \tag{58}$$

Again referring to [22], uncompensated phase errors of this type may not exceed $-25\,\mathrm{dB}$ for sidelobes at frequencies near the mainlobe and $-35\,\mathrm{dB}$ for sidelobes higher up. Thus, to form a high quality SAR image without any compensation methods with the TI AWR1843 with center frequency 79 GHz, the amplitude of vibrations should stay below $30\,\mu\mathrm{m}$ for low frequency sinusoidal errors and $10\,\mu\mathrm{m}$ for high frequency sinusoidal errors.

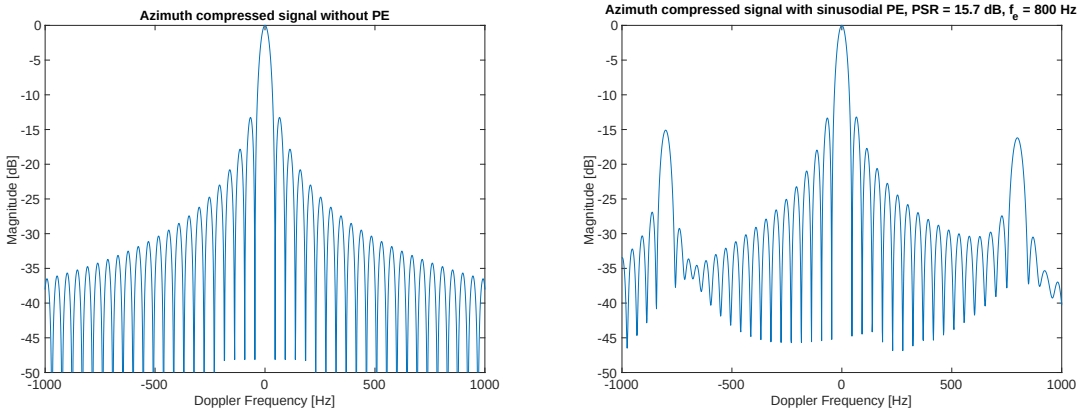

(a) (b)

Figure 14: Azimuth cut showing the compressed SAR signal without and with sinusoidal phase error (left and right, respectively).

2.5.2 Phase Error due to Approximations in Backprojection

In many papers that discuss backprojection for FMCW systems such as [9], [13] and [18], the only phase term that is realized in the matched filter is the Doppler term. This is also what we have presented in the block diagram in Figure 13. Effectively, the residual video phase term is approximated as a phase constant for each pixel. However, this approximation is not obvious since the remaining error is both non-linear and spatially variant, and the approximation therefore requires motivation given here. The magnitude of the phase error is given by

$$\phi_e = \pi S T_s \tau_{m,k} + \pi S \tau_{m,k}^2. \tag{59}$$

The time dependency of $\tau_{m,k}$ follows from (46), where we assume the antenna moves with constant velocity along the x-axis, $a_m = v_x \cdot mT_c$. By expanding (59) we get

$$\phi_e = \pi S \cdot \left(\frac{2T_s \cdot \sqrt{y_k^2 + (x_k - v_x \cdot mT_c)^2}}{c} + \frac{4 \cdot \left(y_k^2 + (x_k - v_x \cdot mT_c)^2 \right)}{c^2} \right). \tag{60}$$

By keeping k fixed and varying m, we can examine the residual video phase error over the aperture for a particular target. A conservative metric of the phase variation is the absolute difference between the maximum and minimum value of ϕ_e. In Figure 15 we have plotted that metric for targets at ranges and angles of interest to automotive SAR using the system parameters defined in Table 6. It should be noted that we present the result using polar coordinates with the angle defined as in Section 2.4.2, i.e. relative to the velocity vector of the radar.

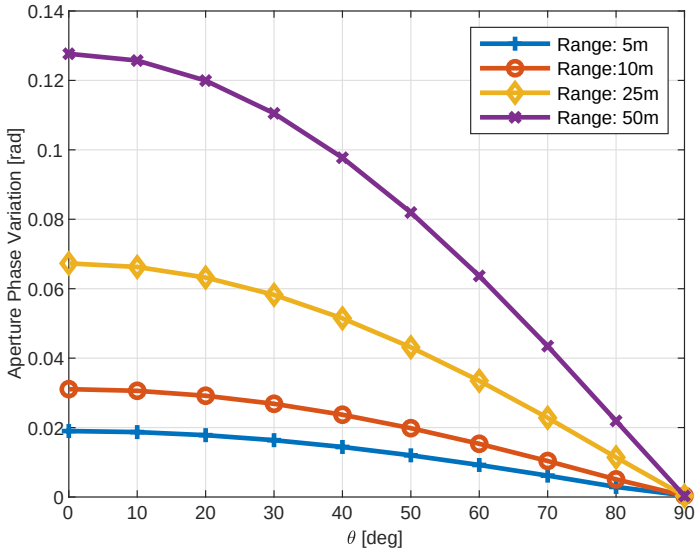

Figure 15: Graph displaying the absolute difference between the maximum and minimum value of the residual video phase term for targets at various angles and ranges of interest for automotive SAR. The angle is measured relative to the velocity vector of the radar and the radar parameters is given by Table 6.

Following the guidelines in [22], a generally accepted rule of thumb for allowable uncompensated quadratic phase errors is $\pi/4$, which is clearly much larger than the maximum residual video phase error seen in automotive SAR. Thus, its imaging effects will most likely be minor and in the rest of the report we will treat the residual video phase as being constant.

2.5.3 Phase Gradient Autofocus

To combat image degradation due to phase errors, one can apply autofocus algorithms to estimate and correct for such errors [23]. In this work, one of these algorithms called phase gradient autofocus (PGA) has been studied and applied to radar data. The main goal of PGA is to estimate the derivative (or gradient) of the phase error, $\dot{\phi}_e$, as accurately as possible, and then integrate it to yield the estimated phase error ϕ_e. The algorithm relies on the assumption of ϕ_e being spatially invariant [23].

An outline of the algorithm used in this thesis work is presented in Figure 16, and was inspired by the descriptions of PGA given in [23], and [24].

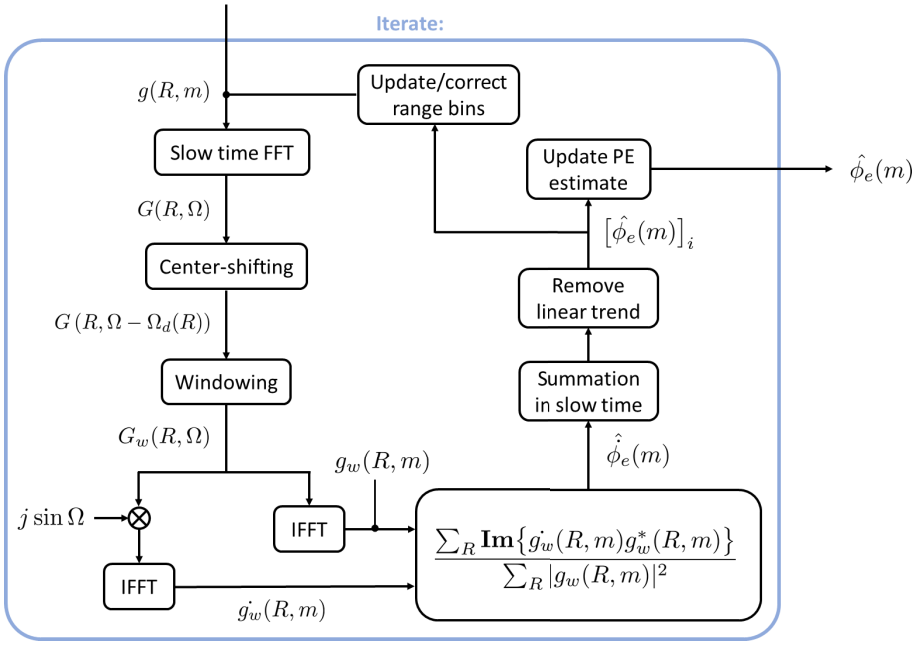

Figure 16: A flowchart showcasing the steps involved in PGA.

The input $g(R,m)$ is a selection of range bins (R is fixed) from range compressed data containing strong scatterers. It is assumed that $g(R,m)$ inhibits a desired, linear phase term in slow time (a Doppler frequency) with the addition of undesired higher order phase terms which constitutes the phase error to be estimated [23],[24]. The algorithm assumes no range migration, and operates in the slow-time dimension where the phase error is most noticeable.

The estimation process occurs iteratively, where the i:th iteration produces a residual phase error $[\hat{\phi}_e(m)]_i$ as shown in Figure 16. The residuals decrease in energy after each iteration, as $g(R,m)$ is corrected with the most recent information before each cycle starts anew. The final phase error estimate is the sum

$$\hat{\phi}_e(m) = \sum_i [\hat{\phi}_e(m)]_i \tag{61}$$

and correction of the image data is achieved by multiplying all range compressed data $S(R,m)$ by a factor

$$S(R,m)_{\text{corrected}} = S(R,m)e^{-j\hat{\phi}_e(m)}. \tag{62}$$

This algorithm is implemented as an intermediate step in the DBS algorithm; it takes place in between range compression and Doppler/azimuth processing.

3 Methodology

In order to answer the research questions of this thesis work, the following method is divided in three parts:

1. Initial measurements using a stationary AWR1843 radar, applying conventional automotive radar processing methods. Such measurements were required to verify the system resolution in R, v_r and θ_a with theory, and to produce images representative of a state-of-the-art automotive radar system which would be compared to the project's proposed SAR system.
2. A simulation of the AWR1843 system used in the project, in order to generate simulated radar data in a quick and easy manner. Simulated automotive SAR scenarios were used to prototype and evaluate imaging algorithms.
3. Practical automotive SAR measurements using real data from the AWR1843, which were then analyzed and evaluated according to the thesis statements.

The first and last part involve real measurements with the AWR1843BOOST evaluation board connected to a DCA1000EVM data capture card. In order to access the data from a PC, both cards were connected to Texas Intruments' mmWave Studio software which in turn was controlled from Matlab. Radar control commands were sent in order to set radar parameters as well as trigger measurements. Radar data from the capture card was recorded with mmWave Studio and loaded into Matlab for processing. For each power cycle of the hardware, communication between the PC and the two cards had to be established in mmWave Studio directly as well as initialization of the hardware before any measurements were possible. A diagram illustrating the setup is shown in Figure 17.

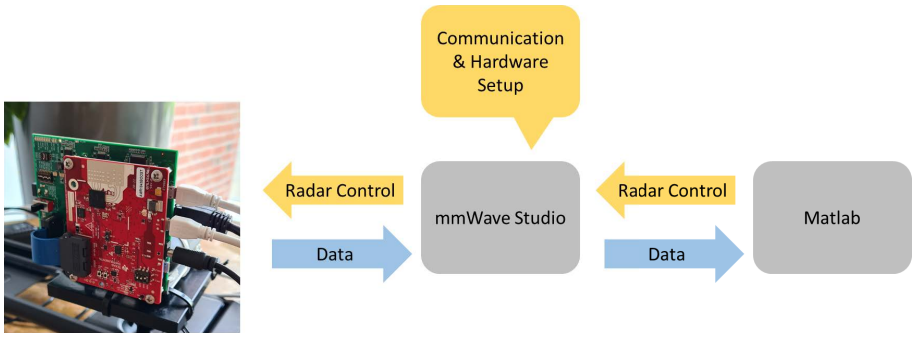

Figure 17: Diagram illustrating the AWR1843 control setup.

3.1 Automotive Processing of Stationary Radar Measurement Data

A set of stationary radar measurements were performed, and the resulting data was processed in line with the theory presented in Section 2.3. Specifically, the algorithms in Figure 8 were used for producing RV- and RA-maps in Matlab. 2D-FFTs were performed using Matlab's `fft2()`-function, working on two different cuts of the IF signal data cube

for respective maps as illustrated in Figure 8. The polar to Cartesian mapping could be done with the `pol2cart()`-function working on the MIMO image data. Resulting surfaces were displayed as power images, normally using the `imagesc()`- or `pcolor()`-functions, measured in decibels relative to the maximum value.

Measured scenes contained metallic triangular trihedral corner reflectors, which are targets usually used for calibrating radars [25]. Reflectors of two different sizes were available as shown in Figure 18. Shortest sides of the large and small reflectors were measured at 28.0 cm and 6.5 cm respectively. The size difference corresponds to an approximate 25 dB difference in radar cross section (RCS), where the larger target has the larger RCS. The reflectors were expected to deliver point target-like responses, such that mainlobe widths and system resolution could be deduced from measurements. This assumed property was also used in SAR measurements described later.

Figure 18: Reflectors used in measurements.

3.2 Simulated SAR Imaging

Three main components of the automotive SAR system had to be identified in order to generate simulated radar data in Matlab:

- The scene to be imaged.
- The radar and its parameters.
- The influence of the physical channel on the received signal amplitude and phase.

The latter is of course a consequence of the first two, since the physical channel is determined by the targets in the scene and their relative positions to the radar. All "targets" in simulations always refer to point targets, defined only by their 3D coordinates $\vec{p}(t) = (x(t), y(t), z(t))$ and a constant, angle of incidence-independent radar cross section σ.

An illustration of a simulated scenario is shown in Figure 19.

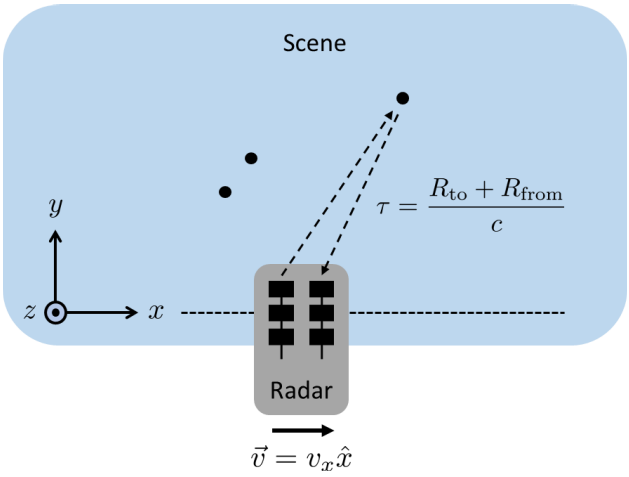

Figure 19: An overview of the automotive SAR simulations. A transmitting and receiving antenna pair represents the radar as it travels along the dashed line trajectory, and observes the scene containing point targets indicated by black dots. Dashed arrows indicate the waveform propagation path, and the resulting delay is indicated to the right.

The above Figure 19 can be thought of as a snapshot at one simulated time instance, whereas the radar position (and sometimes target positions) change over time. The radar is represented here by a transmitting and receiving antenna pair. This is to emphasize that the delay experienced at the receiver is actually the time it takes for the waveform to propagate from the transmitting to the receiving antenna phase center. The simulated "radar position" is hence the positions of six antenna phase centers forming eight such pairs because of the 2×4 MIMO configuration in azimuth. The simulated radar trajectory was normally set on the x-axis, but sometimes a time-varying y-component was applied to simulate motion errors.

3.2.1 Generating the IF Signal

An initial approach of simulating the full signal/waveform chain depicted in Figure 3 was first tested, but rather quickly abandoned as the amount of generated data was too large. This fact, amongst other aspects, motivated direct synthesis of the IF signal $s_{\text{if}}(t)$ instead. For one transmitting (TX) and receiving (RX) antenna pair, this involves computing the right hand side of (14) at each time instance (n, m) for each point target in the scene. The received IF signal is then the superposition of such components:

$$s_{\text{if}}(n,m) = \sum_k \frac{\alpha_k}{2} \exp j\left(2\pi S \tau_{n,m}^{(k)}(nT_s - T/2) + 2\pi f_c \tau_{n,m}^{(k)} - \pi S(\tau_{n,m}^{(k)})^2\right) \tag{63}$$

where α_k and $\tau_{n,m}^{(k)}$ are the attenuation factor and the delay belonging to the k:th target respectively. The delays are calculated as shown in Figure 19, where the TX-to-target range $R_{\text{to}}^{(k)}$ and the from-target-to-RX range $R_{\text{from}}^{(k)}$ are given by

$$R_{\text{to}}^{(k)}(t) = \|\vec{p}_k(t) - \vec{a}_{\text{tx}}(t)\| \tag{64}$$

$$R_{\text{from}}^{(k)}(t) = \|\vec{a}_{\text{rx}}(t) - \vec{p}_k(t)\| \tag{65}$$

where $\vec{p}_k(t)$ is the k:th target position. The vectors $\vec{a}_{\text{tx}}(t)$ and $\vec{a}_{\text{rx}}(t)$ are transmitter and receiver antenna positions, respectively. Thus, for a specific target and antenna pair, we get the delay history computed at each time instance

$$\tau_{n,m}^{(k)} = \frac{R_{\text{to}}^{(k)}(t) + R_{\text{from}}^{(k)}(t)}{c}\Big|_{t=nT_s+mT_c}. \tag{66}$$

It should be noted that simulations themselves do not apply a start-stop approximation, as is done in the context of processing and mentioned in Section 2.4.3. This is since $\tau_{n,m}^{(k)}$ is calculated for all sampling instances and varies slightly even within chirps (in fast-time).

The amplitude factor is taken as the square root of the received power

$$\frac{\alpha_k}{2} = \sqrt{P_{\text{rx}}^{(k)}} \tag{67}$$

where $P_{\text{rx}}^{(k)}$ can be written

$$P_{\text{rx}}^{(k)} = P_{\text{tx}} G_{\text{tx}}^{(k)} G_{\text{rx}}^{(k)} \frac{\lambda^2}{(4\pi)^3 R_k^4} \sigma_k L^{-1} \tag{68}$$

where P_{tx} is the peak transmitted power, $G_{\text{tx}}^{(k)}$ and $G_{\text{rx}}^{(k)}$ are target-dependent transmitting and receiving antenna directive gains, R_k is the range calculated as half the total propagation path, σ_k is the target RCS and L is a loss factor of the receiver. The above expression is a rewrite of (1.19) in [26], where $G^2 = G_{\text{tx}}^{(k)} G_{\text{rx}}^{(k)}$. The transmit power and loss factor are assumed to be unity, while σ_k is defined with the specific target and can hence vary over different targets and scenes.

The simulations employed an analytical model for the 3D antenna gains based on a single MIMO antenna element. The element in itself is composed of three microstrip patch antennas connected in series, forming a three-element array. Without going too much into detail on antenna theory, the patch radiation pattern or directive gain $G_{\text{patch}}(\theta, \varphi)$ was modeled according to [27] using the AWR1843 dimensions and material properties. Here θ and φ denote the angles of a spherical coordinate system referenced at the antenna phase center. The patch pattern was then multiplied with an array factor to form the MIMO element pattern:

$$G_{\text{tx}}(\theta, \varphi) = G_{\text{rx}}(\theta, \varphi) = G_{\text{patch}}(\theta, \varphi) \left|1 + 2\cos\left(k d_x \cos\varphi \sin\theta + \beta d_x\right)\right|^2 \tag{69}$$

where $k = 2\pi/\lambda$ is the wavenumber in free space, d_x is the patch spacing and β is the propagation constant of the connecting microstrip lines. The patches are located along the x-axis of the antenna-centered coordinate system. The pattern was normalized to a maximum directive gain of one. To calculate $G_{\text{tx}}^{(k)}$ and $G_{\text{rx}}^{(k)}$, relative angles θ and φ to the target had to be calculated for both transmitting and receiving antennas at each time instance and then input to the pattern function in (69).

The last step was to add complex, white Gaussian noise to $s_{\text{if}}(n, m)$ at each receiver antenna in accordance to [1] to simulate thermal noise. The noise variance σ_w^2 could be chosen freely, and was never calibrated to match the AWR1843 system.

The procedure of generating the IF as described here is repeated for all simulated channels, of which there can be eight in total. The IF signal is then structured in a 3D matrix as

the data matrices of all channels are stacked on top of each other, and output as the raw, simulated radar data. Most of the time, only one channel output was required. Hence, an option to only simulate one TX-RX pair was also implemented, producing only a 2D data matrix as output.

3.2.2 Implementing and Running Simulations in Matlab

Simulations were built from the ground up and performed in Matlab. Because of its complexity, the simulation software was implemented in a modular fashion meaning that different calculation tasks were split into a number of Matlab functions. Complex entities such as the scene to be imaged and the radar with its many parameters where programmed as structure arrays, in order to carry their information over the various functions in a compact manner.

Before running the simulation, the user had to define a set of parameters and input options which initialized the scene and radar structs. Such parameters and options include target positions, target RCSs and target velocities for the scene, and important radar parameters such as center frequency f_c, sampling frequency f_s, chirp rate S, the CPI and radar platform velocity v_x. After initialization, the simulation software was ready to generate the IF signal as described. To do this, the appropriate functions were called with the radar and scene structs as arguments using a main script in order to generate the data matrix. No other hardware was required except for the authors' PCs.

3.2.3 Verifying and Analysing Simulated Data

The simulated data was continuously verified against the AWR1843BOST module and theory. Verification steps consisted of processing data from simple, easily verified simulated and real scenes using a stationary radar. The processing and presentation of simulated data were conducted exactly as described for measured data in Section 3.1. Results were compared with main focus on the achieved resolution and sidelobe levels.

Once verified, simulations of automotive SAR scenarios were conducted. The data was analysed using BP and DBS image formation algorithms implemented in Matlab following the descriptions given in Section 2.4. The resulting power images, $I(x, y)$, were presented in decibels relative to the maximum value for SAR simulations also.

3.3 Experimental SAR Imaging with the AWR1843

To connect the results found from theory and simulations with reality, a set of SAR experiments were conducted with the AWR1843 radar. To verify the theoretical findings in an idealized environment, a prototype version of automotive SAR was considered first, using a camera slider to generate the sensor motion. After that a more realistic set of experiments were conducted with the radar mounted on an actual vehicle.

3.3.1 Experiments with SAR on a Camera Slider

For the purpose of this project, a motorized camera slider was acquired and used as a prototype platform to generate the desired motion of the SAR sensor. The set-up can be seen in Figure 20 where the radar is mounted on the camera slider which in turn is fixated on a tripod. The camera slider could generate a nearly ideal constant velocity across its length of 41 cm and was controlled via Bluetooth. It should be noted that the maximum velocity of the platform was 3.2 cm/s which is far from what we would want in an automotive scenario. To handle that and still obtain an aperture length and a cross-range resolution that would be representative of an automotive use case, a considerably larger temporal separation between chirps needed to be used. The coherent processing interval used with this system was therefore considerably larger than what would be the case in an automotive use-case.

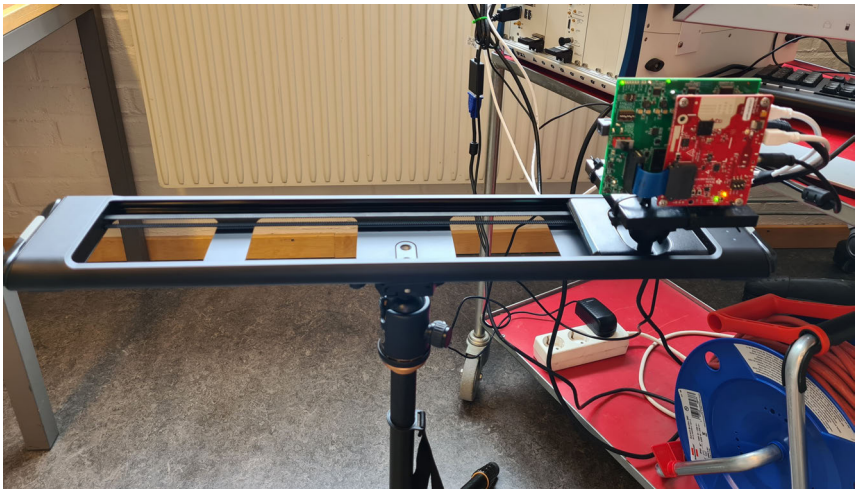

Figure 20: Measurement set up for prototype SAR imaging using a motorized camera slider mounted on a tripod. The camera slider was capable of producing a maximum velocity of 3.2 cm/s and was controlled via Bluetooth.

When collecting the data with the camera slider, the radar was triggered manually with the intention of keeping the aperture center near the central point of the camera slider, where all the scenes had their origin. The scenes that where imaged with this set-up included indoor scenarios with trihedral reflectors of the kind displayed in Figure 18 as well as various outdoor scenarios from the Chalmers campus area. The collected data was then used as inputs to the image formation algorithms described in Section 2.4 and the resulting images were then displayed and analyzed with the `pcolor()`-function. In particular, the system was used to verify the theoretical results on range and cross-range resolution with point target-like responses from earlier described reflectors mounted on tripods at the same height as the antennas. Backprojection in combination with rectangular windowing was the preferred choice when resolution was investigated. Because of the large separation between chirps, MIMO processing with 8 channels could be performed with the same data set meaning that one could directly compare SAR and MIMO images afterwards side by side.

3.3.2 Experiments with SAR on an Actual Vehicle

Automotive SAR measurements from a camera slider can only be made representative to a certain degree. Errors that arise due to imperfect knowledge of the radar's velocity during measurement or antenna vibrations at relevant frequencies are examples of effects that could not be accurately explored with a camera slider. Thus, in order to perform imaging with a more realistic system, the company Veoneer that supported this thesis, gave us access to their test site in Vårgårda and helped us to equip a car with a side looking radar as is shown in Figure 21. The radar was mounted on a wooden platform in front of the bumper and was elevated so that its antenna plane coincided with the height of the fender in a normal car ($\approx 70\,\text{cm}$).

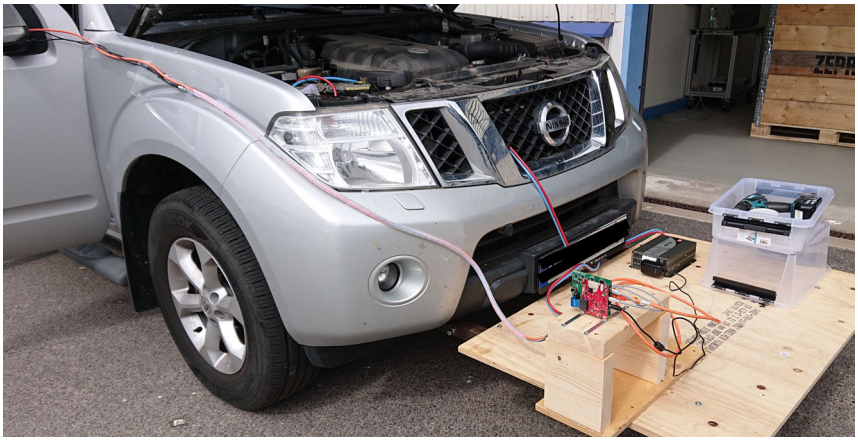

Figure 21: Measurement set up for car mounted SAR. The radar is mounted so that it coincides with and observes a horizontal plane at roughly the same height as the fenders on a normal car ($\approx 70\,\text{cm}$).

The experiments where carried out at Veoneer's test site, which also serves as an airfield for smaller aircraft. To collect relevant data, a variety of scenes was considered with both simple targets, consisting of aluminum foil-clad tubes or more complex "real" targets such as cars or bikes. The radar motion was generated by the car which was driven approximately straight with an intended velocity of either $10\,\text{km/h}$ or $30\,\text{km/h}$ and the measurements were triggered manually from the passengers seat as is shown in Figure 22.

Figure 22: Data acquisition for car mounted SAR. The car was driven approximately straight next to a predetermined scene with velocities 10 km/h or 30 km/h. The radar was triggered manually from the passengers seat when the radar was estimated to be near the scene origin.

The car velocity was measured with the car's speedometer which in retrospect turned out to be an inaccurate method to produce good SAR images. The effect from forming SAR images with an incorrect velocity follows from (39) and essentially means that all Doppler shifts are perceived incorrectly by the imaging algorithms. In essence, if the estimated velocity is too small the off boresight targets will be shifted in azimuth outwards from the scene center and correspondingly, if the estimated velocity is too high the off boresight targets will be shifted in azimuth towards the center. Luckily, in all of the scenarios considered in this report, the imaged scenes had well known inter-distances between objects which thereby made it possible to correct for the error afterwards. The process of correcting the erroneous velocity measurement was made manually and iterated until the stationary objects where located at their known positions and is depicted in Figure 23.

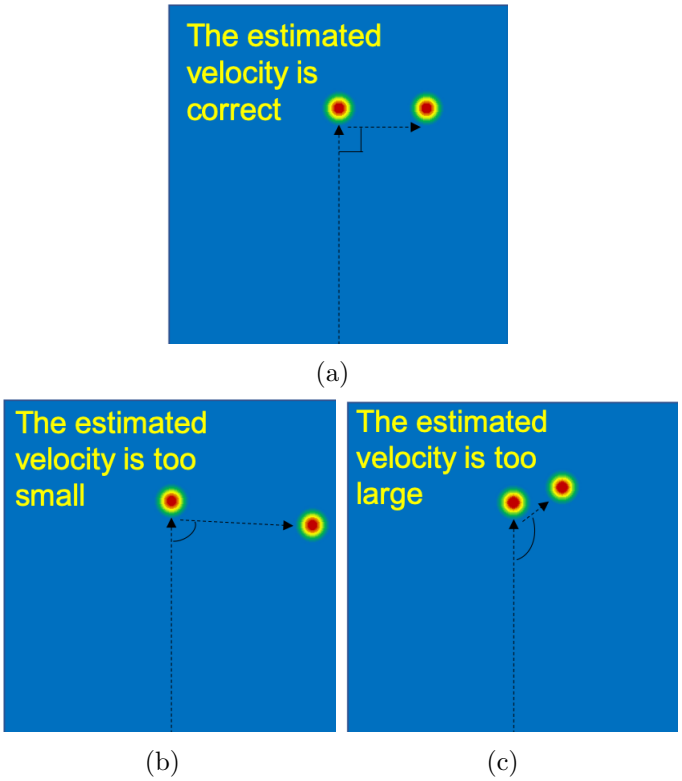

Figure 23: Imaging effects from estimating the radar velocity differently in a scene where two targets have the same y-coordinate. In (a) the correct velocity is used in image formation meaning that angles gets mapped correctly. In (b) the estimated velocity is too small meaning that any off-boresight targets gets shifted in azimuth towards the scene center. Correspondingly in (c) the estimated velocity is too high meaning that any off-boresight targets gets shifted in azimuth away from the scene center.

Lastly it should be pointed out that this process took place after the measurements were done and velocity corrections were made on the order of magnitude $1-5\,\mathrm{km/h}$ for each SAR image. Thus D_{SAR} varied in the actual measurements from what the system parameters suggest but CPI always remained the same. Moreover, the position of the aperture center could not remain constant either because of the manual triggering process. This had the effect that the absolute target position in an image changed each time an experiment was repeated. However, for the measurements considered in this section those effects were deemed to be unimportant.

3.3.3 On Selecting System Parameters for Automotive SAR

In this section we will formulate a method on how to select suitable parameters for the thesis-specific automotive SAR system. The main issue is that aliasing can occur in both signal dimensions which puts restrictions on the devised system. In essence, the limits are the same as for traditional automotive FMCW systems but for SAR imaging they can be interpreted a little differently.

In (30) and (31) we defined maximum unambiguous range and maximum unambiguous velocity for conventional FMCW processing. In SAR, those relations still holds but we will mostly consider scenes where the relative LOS motion comes from the radar instead. Many of the quantities that appear in (30) and (31) can be considered fixed for a certain radar and a certain image scenario and the equations can therefore be formulated in terms of user defined parameters to the left and scene parameters to the right:

$$\frac{f_s}{S} = \frac{2R_{\max}}{c} \tag{70}$$

$$T_c = \frac{\lambda}{4v_{\max}}. \tag{71}$$

To form an informative image we need a bandwidth that roughly matches our requirements on range resolution. A loose/coarse requirement of this bandwidth is first stated as B_{coarse} based on the desired range resolution given by (28):

$$B_{\text{coarse}} = \frac{c}{2\left[\delta_R\right]_{\text{desired}}}. \tag{72}$$

In reality we want a finite number of fast-time samples N that is restricted by the hardware and the bandwidth that we actually sample is given by

$$B = NT_sS = \frac{N}{f_s/S} = \frac{cN}{2R_{\max}} \tag{73}$$

where we have used (70) in the last step. As $R_{\max}$ is fixed by the desired scene-extent, a choice of N should make sure that $B \approx B_{\text{coarse}}$.

The slow-time sampling interval T_c follows from (71) and can be expanded in terms of a ramp interval and the duration of the idle interval T_i: $T_c = NT_s + T_i$. Thus, after choosing a suitable N and a suitable T_i we can also solve for the fast-time sampling rate using the relation

$$T_s = \frac{T_c - T_i}{N}. \tag{74}$$

However, it should be noted that T_i is partly user defined but there are lower limits since the hardware needs time to settle after each chirp. After determining $T_s = 1/f_s$ we can solve (73) for S to get system parameters that fulfills our rough requirements. The resulting range resolution is then $\delta_R = c/(2SNT_s)$.

In an ideal setting, we would want a cross-range resolution that is equal to the range resolution over the entire image so that all targets can be detected with the same accuracy in all directions. However, this is not possible since the cross-range resolution is given by:

$$\delta_{\text{cr}} = \frac{R\lambda}{2v_xMT_c\sin\theta} \tag{75}$$

which is dependent both upon range and the target angle relative to the velocity vector. Thus we should select one location where they are equal, preferably at boresight where $\sin\theta = 1$ and determine a suitable M so that $\delta_{\text{cr}} \approx \delta_R$.

4 Results & Discussion

Results from various processing tasks in this thesis are presented here, many of which are in the form of power (magnitude square) images or surfaces. These are always presented in decibels referenced to the maximum intensity value. Some results presented was generated using rectangular windowing in order to verify resolution values.

4.1 Processing of Stationary Radar Measurement Data

To verify the automotive processing methods described in Section 2.3.1, a set of measurements were performed in order to extract key parameters using RV-maps and RA-maps. The imaged scene consisted of an indoor environment with a stationary radar and two corner reflectors in the same horizontal plane as the antennas. The intended scenario is shown in Figure 24(a) and as can be seen, the nominal positions of targets in Cartesian coordinates was $(x, y) = (0\,\text{m}, 2\,\text{m})$ and $(x, y) = (1\,\text{m}, 3\,\text{m})$ which for the latter corresponds to the range $R = 3.16\,\text{m}$. In one of the experiments, one of the reflectors was carried by a human with the intention of moving radially away from the radar with a speed of $1\,\text{m/s}$. The other reflector was placed on a tripod and remained stationary at $(x, y) = (0\,\text{m}, 2\,\text{m})$ during the measurement. This situation is shown in Figure 24(b). The radar parameters used in this experiment was adapted for a realistic automotive setting and can be seen in Table 1. To verify the cross-range resolution of the system and its MIMO capabilities, a similar scenario was considered again but with two stationary targets at $(x, y) = (0\,\text{m}, 2\,\text{m})$ and $(x, y) = (1\,\text{m}, 3\,\text{m})$ as can be seen in Figure 24(c). The radar parameters used for this experiment is a little bit different and can be seen in Table 2.

Table 1: Parameters for dynamic scene.

Parameter	**Value**
f_c	78.5 GHz
f_s	8 MS/s
S	40 MHz/µs
N	512
M	255
T_c	85 µs
B	2.56 GHz

Table 2: Parameters for static scene.

Parameter	**Value**
f_c	79 GHz
f_s	10 MS/s
S	66.4 MHz/µs
N	512
L	8
B	3.40 GHz

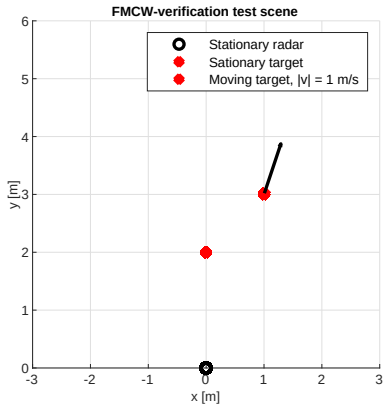

(a)

(b)

(c)

Figure 24: Scene used to verify the FMCW system model in terms of range and velocity measurements. In (a) we see the positions of the two targets, one stationary in boresight at $R = 2\,\mathrm{m}$ and one moving radially away from the radar nominally at $(x, y) = (1\,\mathrm{m}, 3\,\mathrm{m})$. In (b) we see the stationary target in the form of a trihedral reflectors and the measurement tape, which the person carrying the reflector walked on. In (c) both targets are stationary in order to verify the system model in terms of angular measurements using 8 MIMO channels.

The resulting RV-map from the scene described by Figure 24(b), using a rectangular window function, is shown in Figure 25(a). Indeed we have a strong stationary target approximately at $R = 2.1\,\mathrm{m}$ as well as a moving target with speed $v = 1.3\,\mathrm{m/s}$ at $R = 2.9\,\mathrm{m}$. Other large reflections can be seen around $R = 5\,\mathrm{m}$ and $R = 0\,\mathrm{m}$ which likely was the facing wall and mutual antenna coupling respectively. Similarly, the obtained RA-map from the scene described by 24(c) is shown in Figure 25(b). Two strong reflections can clearly be seen with centers at the coordinates $(x, y) = (0\,\mathrm{m}, 2\,\mathrm{m})$ and $(x, y) = (1\,\mathrm{m}, 3\,\mathrm{m})$.

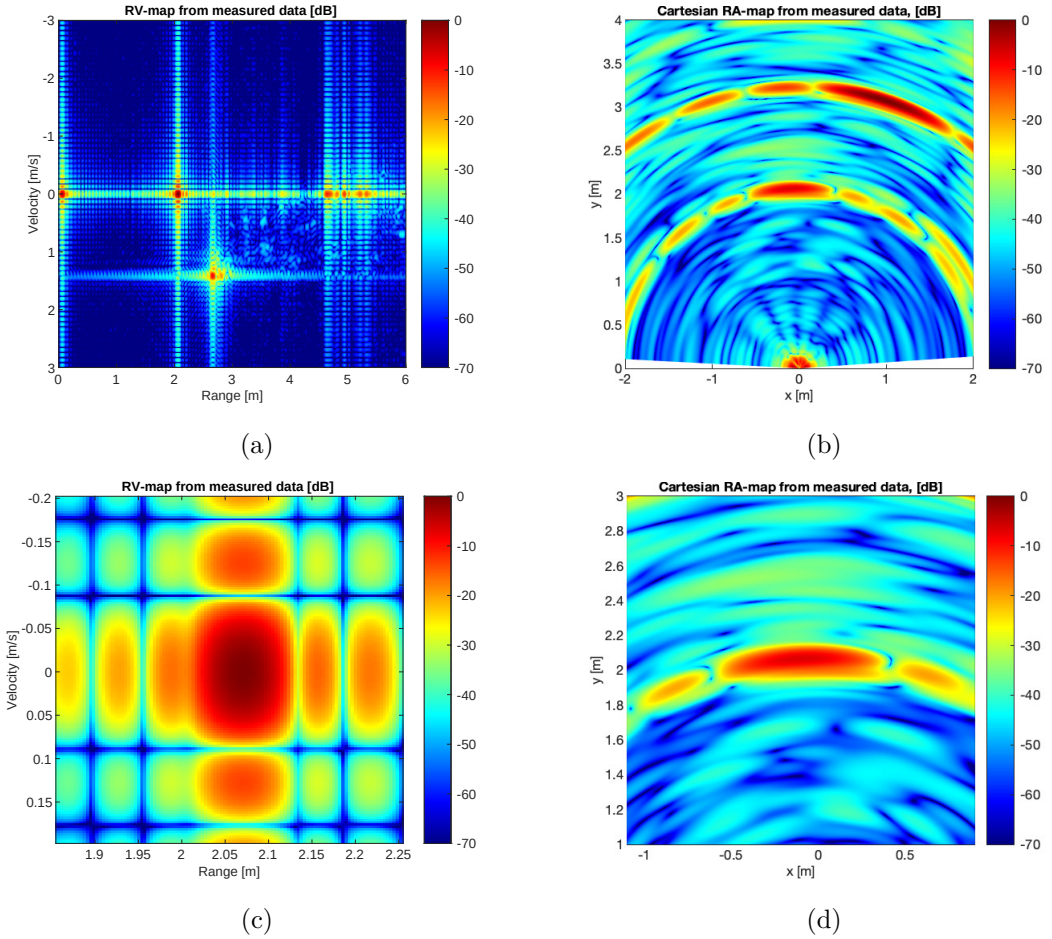

Figure 25: Here we see the result from applying conventional FMCW processing on the captured data from the scenario depicted in Figure 24(a). In (a) we see an RV-map formed with a rectangular window function covering the entire room including the two targets described by Figure 24(b), were one target was stationary and the other was moving. In (b) we see the resulting RA-map, formed with a rectangular window function, from the scenario shown in Figure 24(c) with two stationary targets. In (c) the mainlobe of the stationary target in the RV-map is in focus. Lastly, in (d) the mainlobe of the boresight target in the RA-map is in focus.

In Figure 25(c) the mainlobe of the stationary target in the RV-map is in focus and the calculated range and cross-range resolution compared to what theory suggest from (28) and (29) is shown in Table 3. Here it should be noted that the mainlobe appears to be asymmetric in range which might be explained by energy scattered off the tripod or other irregularities in close proximity of the reflector. It seems the first left sidelobe has merged with the mainlobe, but the half mainlobe width (δ_R) could still be measured. Lastly, in Figure 25(d) the mainlobe of the boresight target is in focus and a comparison with the theoretical results from (33) is shown in Table 3.

Table 3: Measured resolution values from Figure 25(b) compared to theory.

	Measured value	**Theoretical value**
δ_R	6.0 cm	5.9 cm
δ_v	9.0 cm/s	8.8 cm/s
δ_{cr}	50 cm	50 cm

4.2 Simulation Results

Here follows results from the simulations carried out in this work. The simulations are first compared to theory and the AWR1843 system. Then, SAR imaging is performed on ideal and non-ideal simulated automotive SAR geometries.

4.2.1 Verifying Simulation Performance

A quick verification of the simulated MIMO antenna gain pattern is first made. Cuts of the pattern function described by (69) were calculated and compared to values given by Texas Instruments in Figure 12 of [28], and the comparison is shown in Figure 26. These are the $\varphi = 0°$ and $\varphi = 90°$ cuts, known as the E- and H-plane patterns of the MIMO elements respectively.

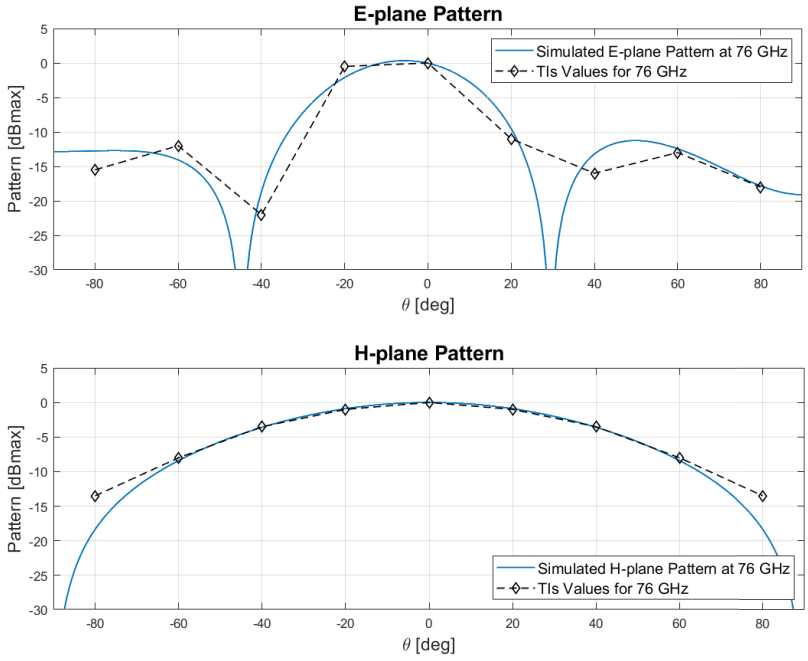

Figure 26: Comparison of E- and and H-plane patterns for the analytical model of MIMO antenna elements versus values given by Texas Instruments [28] sampled at 20° increments. Values are presented in decibels relative the maximum value in both cases.

Results show that the analytical model follows the characteristic provided by Texas Instruments well, especially near $\theta = 0°$ for the H-plane. It should be noted that simulated data most often only considers the H-plane, as it coincides with the xy-plane when the radar is standing upright, i.e. the H-plane is the azimuth slice and the E-plane is the elevation slice of the antenna gain pattern.

Next, the generated data is verified against theory. To do this, a realistic scene consisting of a stationary radar and two point targets was considered, identical to the situation in Figure 24(a). As before, the stationary target resides at $(x, y) = (0\,\text{m}, 2\,\text{m})$ and the initial position of the moving target was determined to be $(x, y) = (1\,\text{m}, 3\,\text{m})$, meaning that its range is 3.16 m. The moving target was also given a velocity with magnitude 1 m/s directed radially away from the radar. The radar parameters used for the simulation verification process is shown in Table 4.

Table 4: Radar parameters used to verify FMCW simulation model.

Parameter	**Value**
f_c	78.5 GHz
f_s	8 MS/s
S	40 MHz/µs
N	512
L	8
T_c	85 µs
B	2.56 GHz

A RV-map formed from the simulated data can be seen in Figure 27(a). Moreover, using the same data cube a RA-map was formed over the 8 MIMO channels as can be seen in Figure 27(b). Clearly, the targets have mainlobes that shows up at the expected positions.

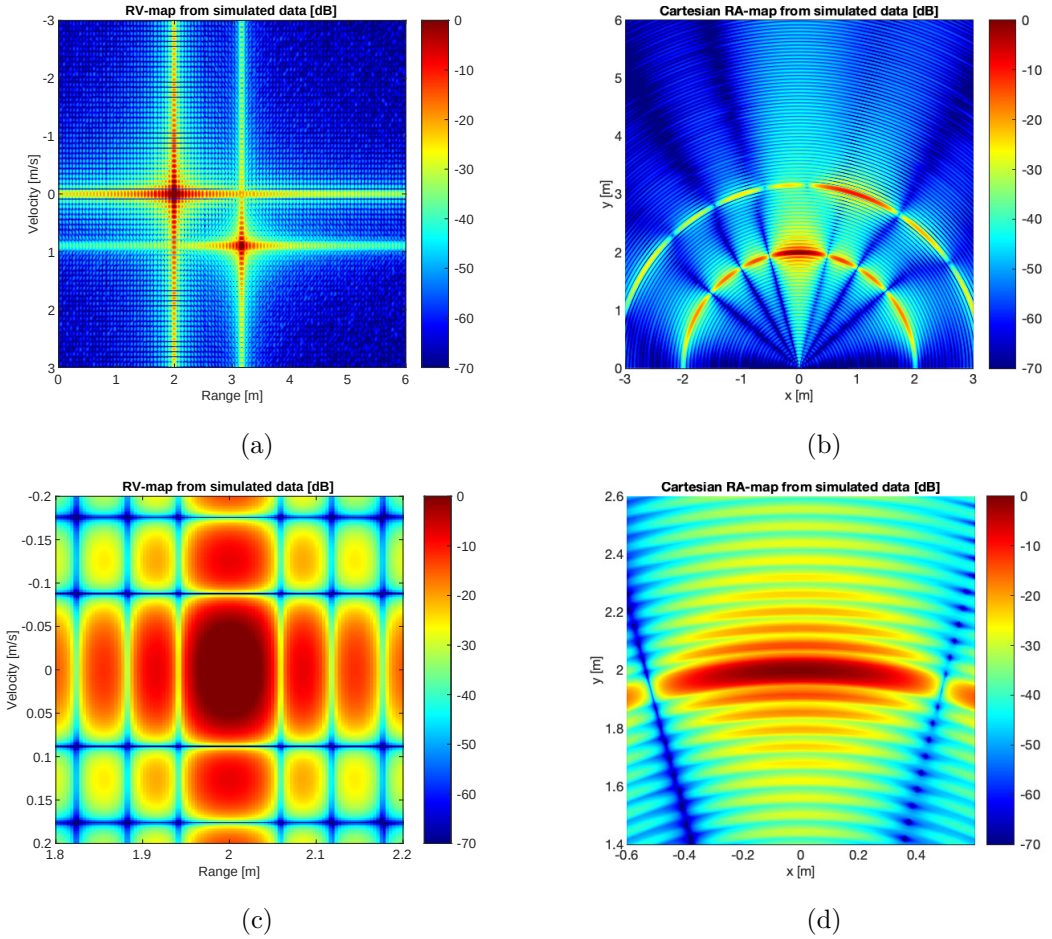

Figure 27: RV- and RA-maps based on simulated data from the scene depicted in Figure 24(a) with one stationary target and one moving target. In (a) we see the overall RV-map over the scene using a rectangular window function and in (b) we see the corresponding RA-map formed with 8 MIMO channels, also with a rectangular window function. In (c) the mainlobe of the stationary target in the RV-map is in focus and in (c) we see the mainlobe of the same target in the RA-map.

Using the theoretical results presented in (28) and (29) and (33) we can calculate the resolution in range, velocity and cross range with the parameters in Table 4 and compare with what can be measured in Figure 27(c) and Figure 27(d). The result is shown in Table 5. From this we conclude that the simulation produces results that agrees very well with theory.

Table 5: Measured resolution values from Figure 27 compared to theory.

	Measured value	**Theoretical value**
δ_R	6.0 cm	5.9 cm
δ_v	9.0 cm/s	8.8 cm/s
δ_{cr}	50 cm	50 cm

4.2.2 Simulated SAR Imaging

Initial SAR imaging attempts were performed on a simple simulated scene containing a strong target at $(x, y) = (0, 3\,\text{m})$, close to boresight. The target is positioned in the xy-plane, in which the radar travels. In Figure 28 is presented a resulting BP image using rectangular windowing. The SAR system parameters used are given in Table 6.

Table 6: SAR system parameter values used in initial SAR simulations.

Parameter	Value
f_c	78.5 GHz
f_s	8 MS/s
S	40 MHz/µs
N	512
M	255
T_c	85 µs
B	2.56 GHz
v_x	10 m/s or 36 km/h
D_{SAR}	21.7 cm

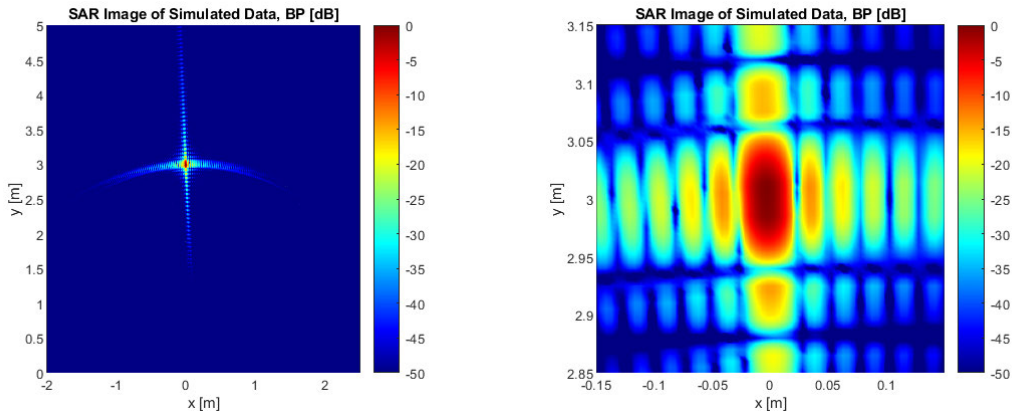

(a) (b)

Figure 28: A SAR image based on simulated data using the backprojection algorithm. The scene is composed of only one point target at range $R = 3\,\text{m}$ almost at boresight. The image was produced using rectangular windowing.

From Figure 28(b) we can measure the half mainlobe widths in both range and azimuth directions to find the resulting resolution values. These values are compared to theoretical ones in Table 7, and it is noted that the resulting range and cross-range resolution agrees well with theory. The theoretical values are calculated using (28) and (53), respectively.

Table 7: Measured resolution values from Figure 28b compared to theory.

	Measured value	Theoretical value
δ_R	6.0 cm	5.9 cm
δ_{cr}	2.5 cm	2.6 cm

Next, a scene containing three targets at the same range of $R = 3\,\mathrm{m}$ but different angles was imaged. Two of the targets had a RCS 25 dB greater than the third, one at approximately boresight and the other at an angle of 40° to the first. The weaker, third target was placed 6° relative to the strong target close to boresight. All targets are located in the xy-plane as shown in Figure 29(a). Three different imaging results are shown in Figure 29. The SAR images in Figure 29(b) and (c) use different windows: rectangular and Hann respectively in both fast and slow time. The MIMO image for comparison in Figure 29(d) is produced from a stationary radar observing the same scene.

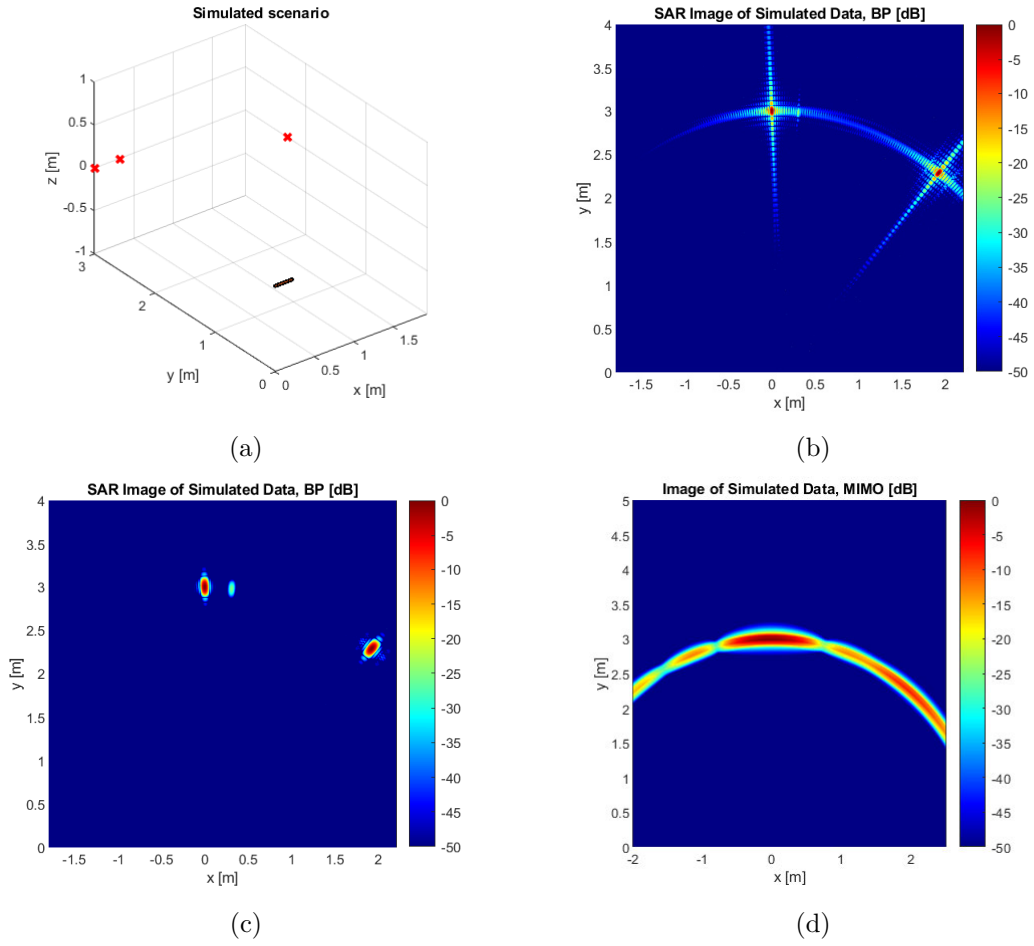

Figure 29: Imaging results of the three-target simulated scene. Red crosses in (a) depict the target positions in 3D-space, while black dots show the radar antenna positions throughout the SAR measurement.

The above Figure 29(b) shows that small targets are at risk of being hidden by large sidelobes from closely located, stronger targets. But, this effect can be supressed by using windows like Hann as shown in Figure 29(c). Also in Figure 29(b) and (c), we see small signs of broadening in cross range of the far out strong target. The half mainlobe measures approximately 3.2 cm, which is 28 % wider compared to the boresight target. The theoretical $1/\sin\theta$ broadening factor in (53) predicts this behaviour rather well since $(1 - 1/\sin 50°) \times 100\,\% = 31\,\%$. Note that while the target is 40° from boresight, its angle relative the velocity vector is 50°, hence $\theta = 50°$ is the correct value to enter in (53). In Figure 29(d) produced using MIMO, we can separate between the two strong targets but

the smaller is not visible which emphasizes the large improvement in resolution of the SAR system. In theory, the boresight SAR angular resolution in azimuth becomes

$$\delta_\theta = \frac{\lambda}{2D_{\text{SAR}}} \cdot \frac{180^\circ}{\pi} = \frac{0.4\,\text{cm}}{2 \cdot 21.7\,\text{cm}} \cdot \frac{180^\circ}{\pi} = 0.5^\circ$$

using $(53)/R$, and is about 4 % of the theoretically promised MIMO resolution in boresight of 14° presented in Section 2.3.4.

The alternative SAR imaging algorithm, DBS, was also tested along with its assumptions in simulations. Remember, the much simpler DBS algorithm assumes no range migration and an approximately constant relative angle θ to a target. Figure 30(a) illustrates an imaging scenario where three equally strong targets are placed out at approximately $(R, \theta) = (1\,\text{m}, 90^\circ)$, $(2\,\text{m}, 60^\circ)$ and $(3\,\text{m}, 90^\circ)$ relative to the synthetic aperture center. Figure 30(b) shows the real part of range compressed data, where the color scaling is set to only show the positive peaks. This is in order to easily view the change in frequency in slow time as m progresses (downwards in the image). Resulting SAR images are presented in 30(c) and (d), in polar and Cartesian coordinates, respectively. Amplitude factor effects such as $1/R^4$-attenuation and the antenna pattern were turned off for this particular simulation to emphasize differences in phase of targets.

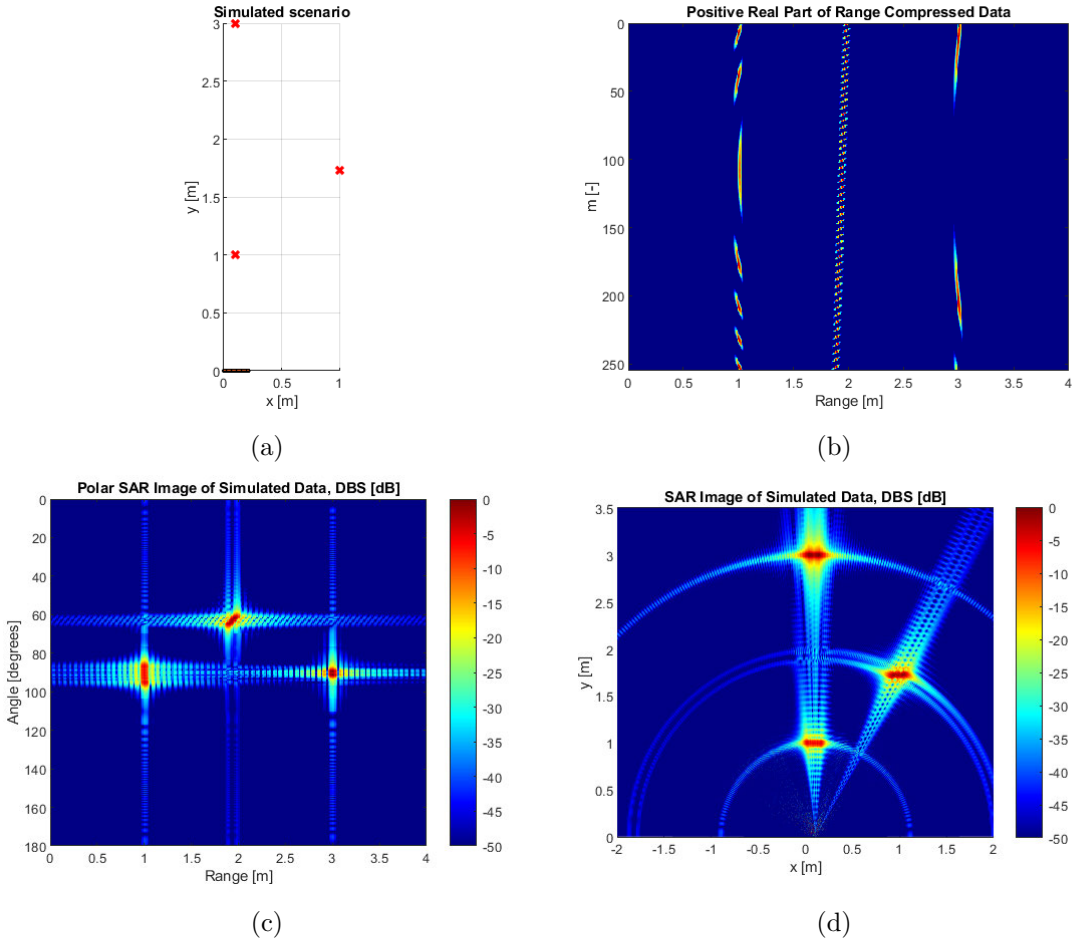

Figure 30: Checking the assumptions of the DBS imaging algorithm and applying it to simulated data. Figure (a) depicts the simulated scene, (b) shows the positive peaks of the real part of range compressed data. Resulting polar and Cartesian SAR images are shown in (c) and (d), respectively.

By observing Figure 30(b), the closest of the three targets show a significant phase modulation indicated by the change in rate of the positive peaks over m. Together with the furthest, it shows signs of going from positive to negative Doppler frequency as the radar passes its x-coordinate but the change happens more slowly for the latter. This results in two different Doppler bandwidths or, equivalently, angular bandwidths as shown in Figure 30(c) where it is also evident that the modulation results in broadening in azimuth. The middle target experiences some range migration, illustrated by the tilt of the corresponding range history in Figure 30(b). The range migration results in broadening in the range direction as seen in 30(c) and (d), and is apparently dependent on target relative angle as well as the length traveled by the radar D_{SAR}.

4.2.3 Simulated Motion Errors

For an automotive use case, the assumption of an ideal radar trajectory perpendicular to the imaged plane during data acquisition might be unrealistic. To study the effects

in SAR images from violating those assumptions, motion errors in the form of antenna vibrations were induced in simulation experiments. The same data was then fed into PGA as shown in Figure 16 to see to what extent the phase error could be mitigated. Since the assumptions of PGA are essentially the same as for DBS, namely no range migration and that the pure signal has an approximately linear Doppler phase term, DBS was chosen as the imaging algorithm in this study. Thus, to isolate the effects from the phase errors due to vibrations, a target at a relatively long range (10 m) was chosen. The resulting SAR image without any phase error is shown in Figure 31(a). However, by applying PGA even without any motion errors being present, as is shown in Figure 31(b), the algorithm tightens the mainlobe in azimuth anyways, indicating that non-linear phase terms are present which we would also expect from an image formed with DBS.

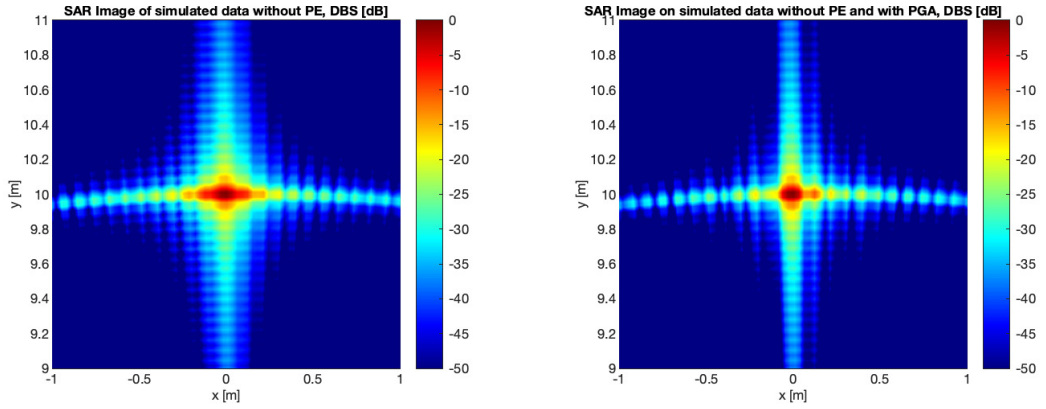

(a) (b)

Figure 31: SAR images based on simulated data with one point target at range 10 m with no induced motion error (a). In (b), the same data set was fed into PGA indicating that non-linear phase terms exist in slow time even without external excitations.

As previously discussed, an antenna vibration corresponds to a sinusoidal phase error of the kind described by (55). The potential imaging effect from such an error would be "ghost targets" which could be highly problematic for ADAS where automatic target recognition is used. In order to study this effect, the return signal from a single point target located at range 10 m directly at boresight was simulated with different combinations of vibration parameters. The company Veoneer that supported this thesis had earlier conducted vibration experiments indicating that the lateral vibrations in a luxury modern car are associated with displacements that are less than 50 µm on normal roads and can be up to 200 µm on rougher roads. The frequency content is generally wide-band and confined in the region 10-100 Hz but in certain situations such as when riding on rumble strips, the power spectral density can have well defined peaks in the region 0-400 Hz. In order to isolate the image effects from single frequency vibrations of this magnitude, simulations was performed with motion error amplitudes of either 50 µm or 200 µm and a vibration frequency of either 100 Hz or 400 Hz. PGA was also applied to the same data in order to evaluate its necessity. The other radar parameters where assigned according to Table 11. The results from the simulation experiment are shown in Figures 32-35.

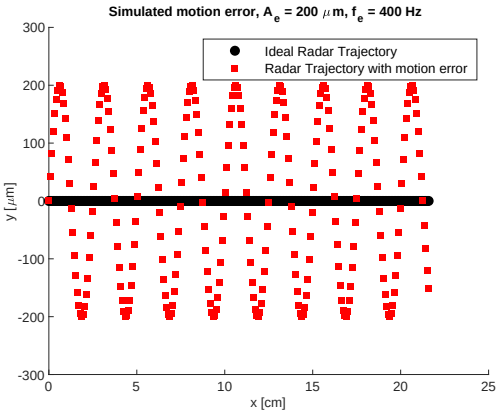

(a)

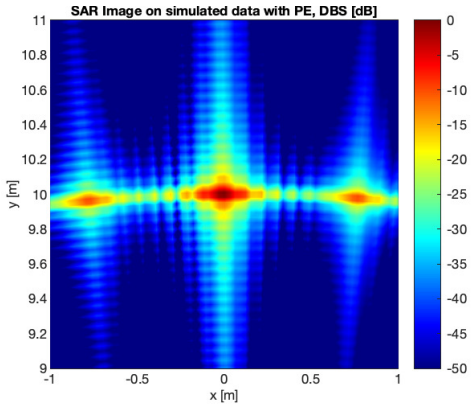

(b)

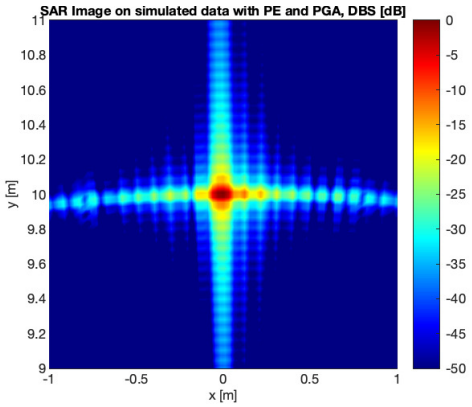

(c)

Figure 32: Radar trajectory (a) with a sinusoidal motion error with amplitude 200 µm and a frequency of 400 Hz. This aims to mimic the extreme case when a car travelling at 30 km/h rides on rumble strips and observes a stationary target at 10 m. The corresponding DBS SAR image is shown in (b) and the effect from applying PGA to the same data before producing an image is shown in (c).

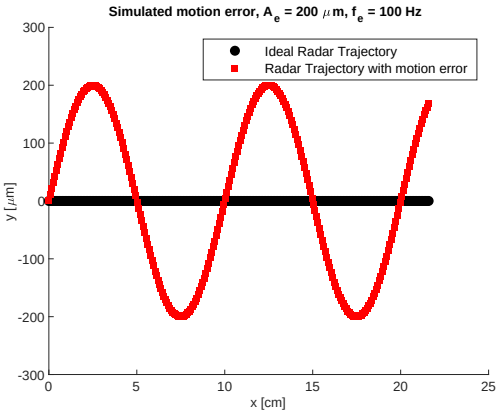

(a)

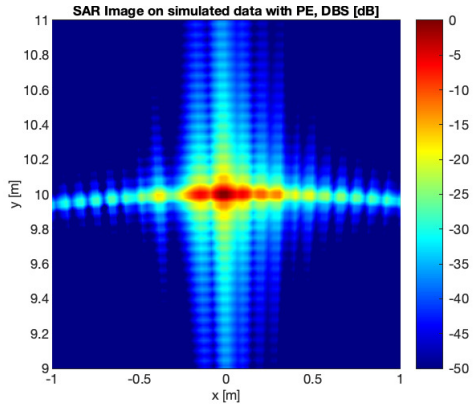

(b)

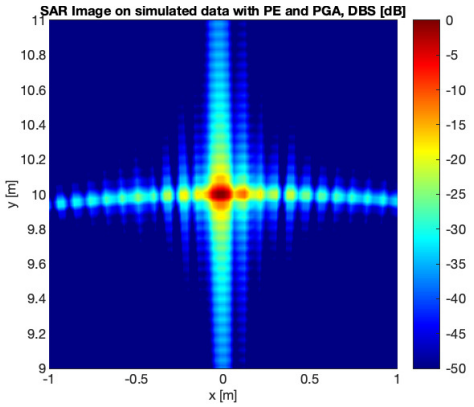

(c)

Figure 33: Radar trajectory (a) with a sinusoidal motion error with amplitude 200 µm and a frequency of 100 Hz. This aims to mimic the case when a car travelling at 30 km/h rides on a rough road and observes a stationary target at 10 m. The corresponding DBS SAR image is shown in (b) and the effect from applying PGA to the same data before producing an image is shown in (c).

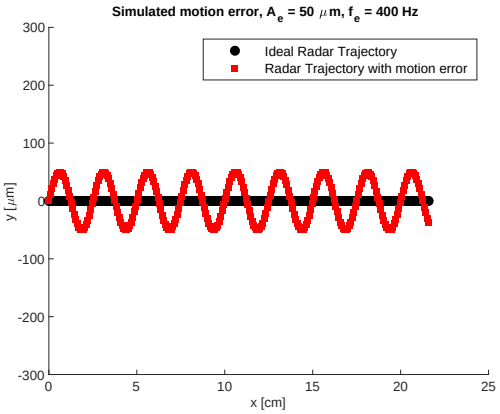

(a)

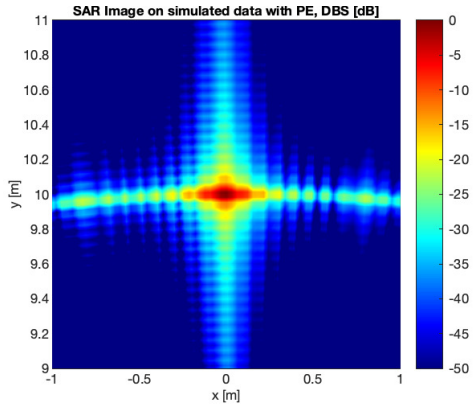

(b)

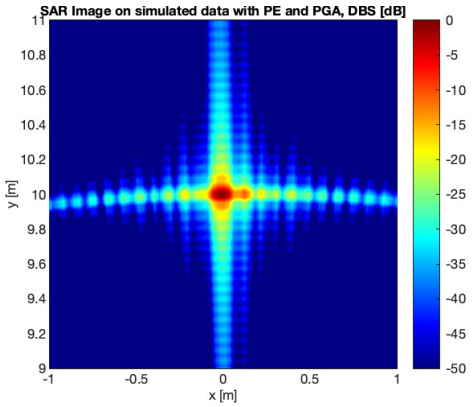

(c)

Figure 34: Radar trajectory (a) with a sinusoidal motion error with amplitude 50 µm and a frequency of 400 Hz. This aims to mimic the case when a car travelling at 30 km/h rides on a road that is normal in terms of lateral displacements but still experience high frequency vibrations while observing a stationary target at 10 m. The corresponding DBS SAR image is shown in (b) and the effect from applying PGA to the same data before producing an image is shown in (c).

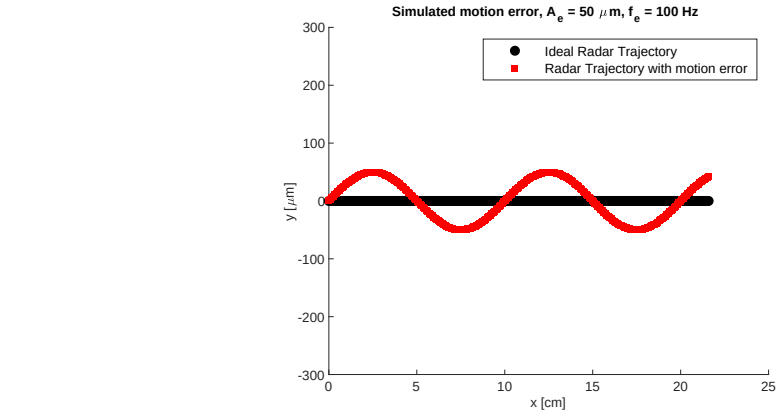

(a)

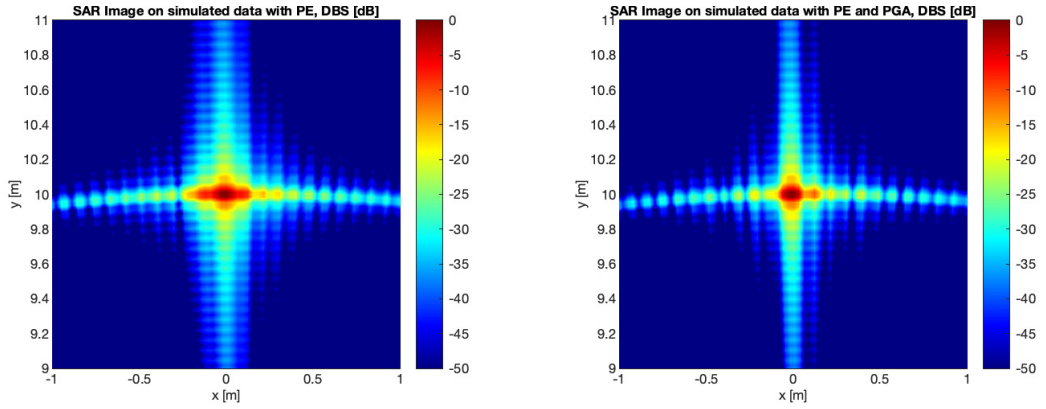

(b) (c)

Figure 35: Radar trajectory (a) with a sinusoidal motion error with amplitude 50 µm and a frequency of 100 Hz. This aims to mimic the case when a car travelling at 30 km/h rides on a normal road while observing a stationary target at 10 m. The corresponding DBS SAR image is shown in (b) and the effect from applying PGA to the same data before producing an image is shown in (c).

By observing Figure 32(b) we see can clearly see the expected result of a single peak at the expected location and a set of paired echoes. With an amplitude of 200 µm, the theoretical PSR follows from (58) and is in this case -9.65 dB which agrees well with the color scale. Following (39), the paired echoes from the vibration frequency 400 Hz should theoretically arise at angles $\pm 4.4°$ from boresight which corresponds to the coordinates $(x, y) = (\pm 0.76, 9, 97)$ which agrees well with the formed SAR image. As can be seen in Figure 32(c) PGA returns an image that is nearly identical to Figure 31(b).

By applying the same reasoning on Figure 33(b) where the vibration frequency is now 100 Hz, the paired echoes should arise at angles $\pm 1.1°$ which explain why they appear to be much closer to the mainlobe, in this case around $(x, y) = (\pm 0.19, 9, 99)$. Again PGA returns an image in Figure 33(c) that is is nearly identical to Figure 31(b).

In Figures 34(b) and 35(b) the amplitude of the vibration was instead 50 µm which is less significant in relation to the radar wavelength. The resulting theoretical PSR is in

that case $-21.69\,\mathrm{dB}$. In Figure 34(b) the paired echoes is just above the sidelobe levels at those coordinates, $(x, y) = (\pm 0.76, 9, 97)$ and in Figure 35(b) the echoes appears to be completely hidden by the mainlobe. Moreover the PGA results in Figure 34(c) and 35(c) are again identical to Figure 31(b).

To conclude those four experiments that aimed to highlight some effects that might arise in an automotive SAR image, riding on rumble strips might produce paired echoes as described in Section 2.5.1. However, the main result from this section indicates that the vibration frequencies experienced on normal roads will not be visible as paired echoes in the traditional sense but rather as a broadening of the mainlobe. The explanation to this is that those frequencies are not much larger than the inverse of the coherent processing interval, which in this case is

$$1/\mathrm{CPI} = v_x/D_{\mathrm{SAR}} \approx 46\,\mathrm{Hz}. \tag{76}$$

However, as can readily be seen from (76), by increasing the velocity or decreasing the aperture length, that number might change. It should also be pointed out that broadening of mainlobes is a serious issue which ultimately limits the cross-range resolution of the system and should therefore be mitigated if possible.

Lastly, it is important to note that sidelobe levels are highly dependent on which type of window that is being used. In all examples shown here we have used a rectangular window but in practice it is often a good choice to use something else. Repeating the simulations made to produce Figure 34(b) but instead using a Hann window we obtain Figure 36(a). Here we can clearly see that the paired echoes are much more prominent in relation to the sidelobe levels. The result from PGA in 36(b) is slightly different this time but one can clearly see that the paired echoes that was previously located at $(x, y) = (\pm 0.76, 9, 97)$ are now gone but we still see some intensity near the mainlobe.

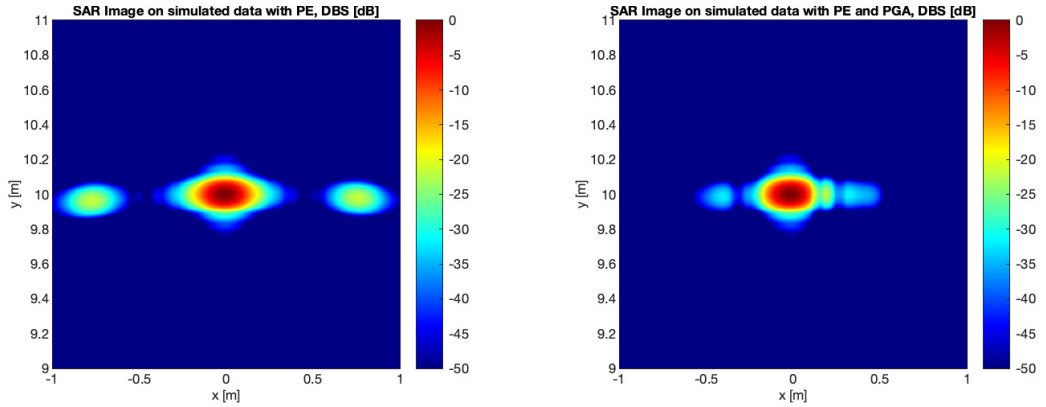

(a) (b)

Figure 36: SAR images with Hann windowing on one simulated point target and a sinusoidal motion error with amplitude $50\,\mu\mathrm{m}$ and frequency $400\,\mathrm{Hz}$. In (b) the effect from applying PGA to the same data set is shown.

4.3 Experimental SAR Imaging

Experimental results using the prototype camera slider-setup are presented first. Then, resulting images produced using the car-mounted setup are shown, analysed and discussed. Images throughout these experiments were formed using both BP and DBS algorithms, but results from both are not always presented for each experiment in order to save space.

4.3.1 Prototype Camera Slider SAR

Here follows some SAR images collected with the camera slider, with SAR parameters listed in Table 8. Note that the slider speed is very small, which motivates a relatively long measurement time of approximately 5 s to achieve a large enough synthetic aperture.

Table 8: SAR system parameter values used in prototype SAR measurements.

Parameter	**Value**
f_c	79 GHz
f_s	10 MS/s
S	66.4 MHz/µs
N	512
M	256
L	8
T_c	20 ms
B	3.40 GHz
CPI	5.1 s
v_x	3.2 cm/s
D_{SAR}	16.4 cm

Initial measurements investigates a similar situation to the simulated scenario in Figure 29, but excluding the far out strong scatterer. A large and a small reflector were placed at $R \approx 3$ m with approximately 6° separation in azimuth as shown in Figure 37(a).

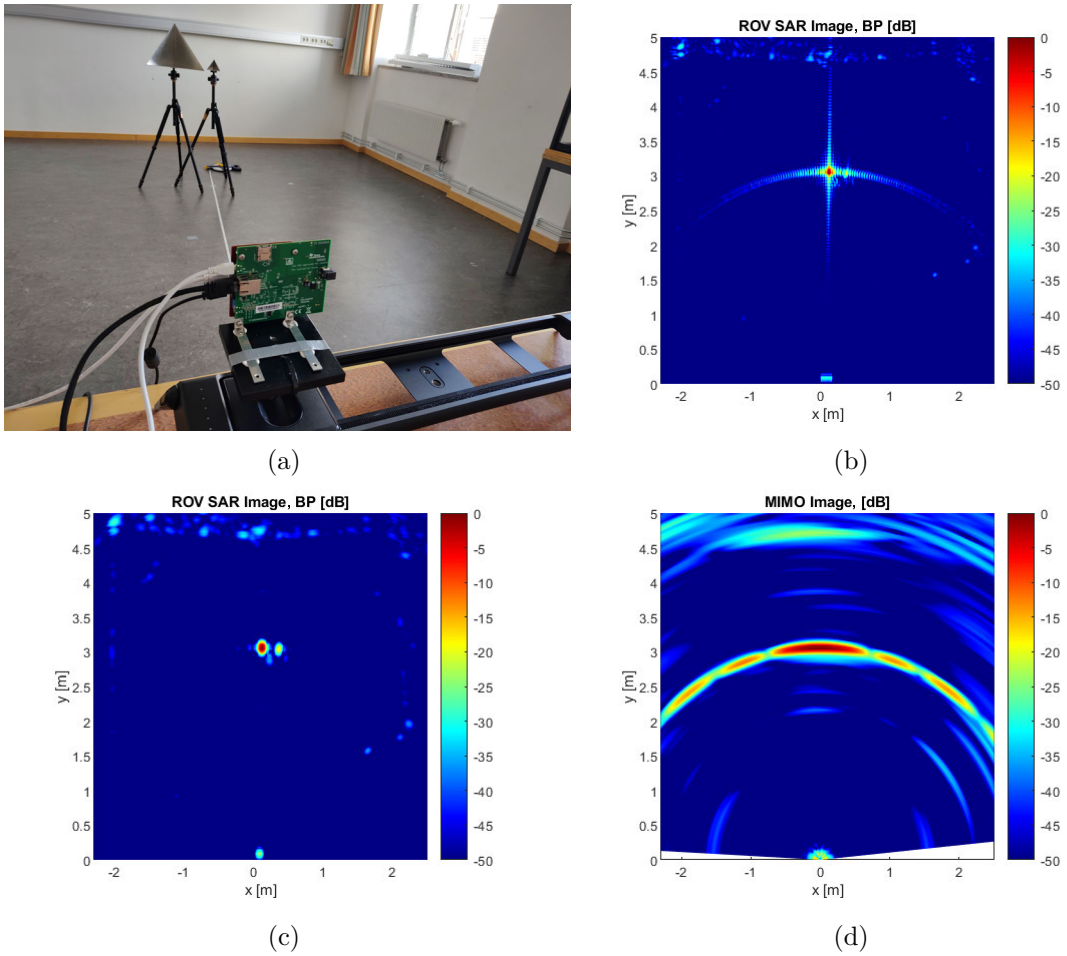

Figure 37: Imaged scene in (a) together with resulting BP SAR images in (b) and (c) using rectangular and Hann windowing, respectively. A MIMO image of the same scene is presented in (d) for comparison.

The above Figure 37(b) and (c) show again the improved resolution of the SAR system over MIMO in Figure 37(d) as predicted by simulations. SAR images were created with the backprojection algorithm using rectangular and Hann windows for Figure 37(b) and (c) respectively, where Hann performs better due to its sidelobe reduction allowing the weak target to be seen. The walls of the room in Figure 37(a) can be seen in the very edges of each SAR image also. Half mainlobe widths/resolution values were measured from the strong scatterer at boresight in Figure 37(b) and compared to corresponding theoretical values produced using (53) in Table 9, which shows that the experimental setup works as expected.

Table 9: Measured resolution values from data presented Figure 37(b) compared to theory.

	Measured value	**Theoretical value**
δ_R	5.0 cm	4.4 cm
δ_{cr}	3.5 cm	3.5 cm

Next, imaging results from a few scenes containing more interesting targets are presented.

First, a closely located, small reflector was placed before a large copper building located at Chalmers and the resulting scene was captured with the radar on the camera slider, as shown in Figure 38. Another small reflector was placed at the base of the building.

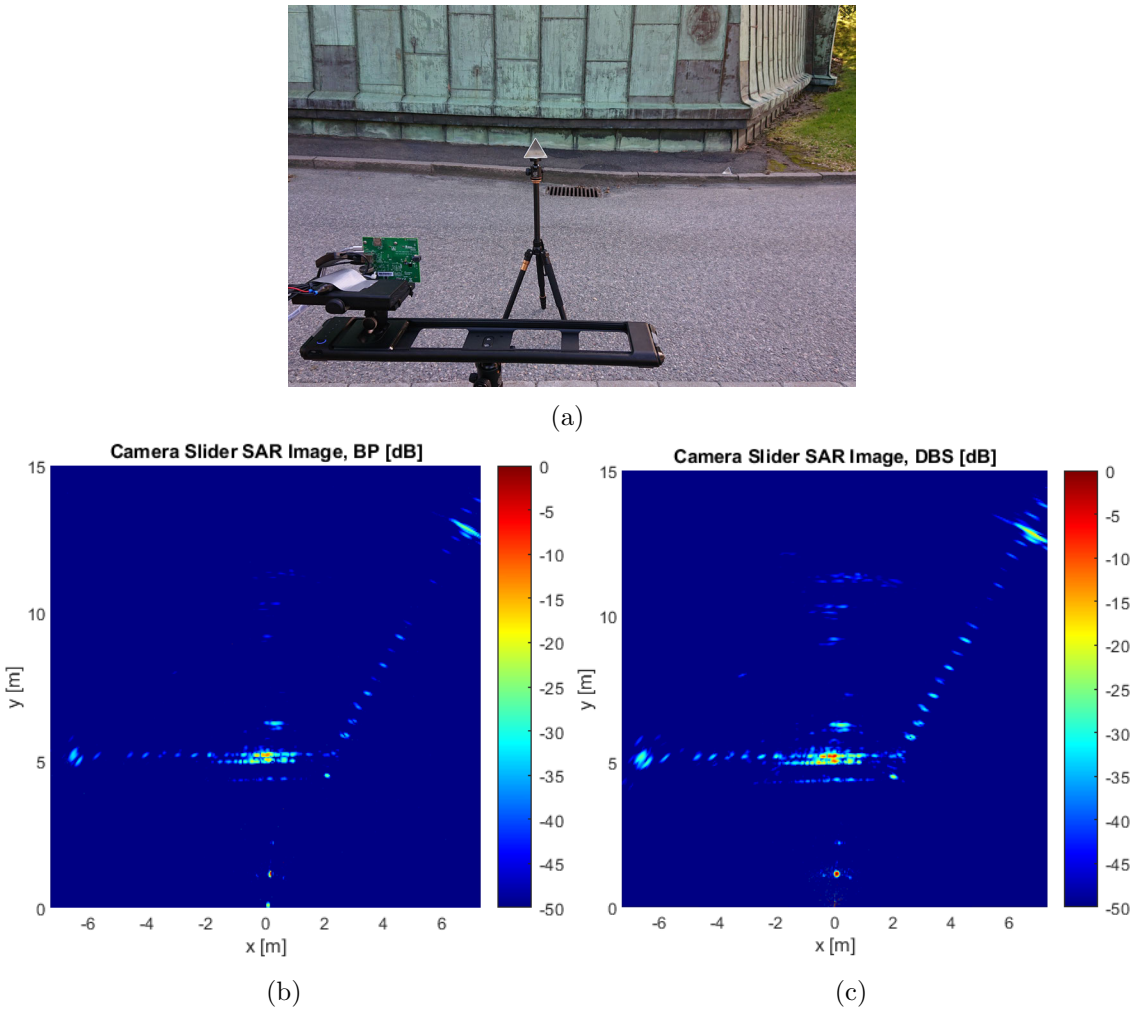

(a) (b) (c)

Figure 38: Camera slider SAR measurement of reflectors in front of a copper building. SAR images (b) and (c) are made with BP and DBS respectively with Hann windowing.

The Figures 38(b) and (c) show that the small reflectors can be detected even when a very large metallic object is present. Also, the response of the close reflector have different widths in cross range for the two images (BP and DBS respectively), which is expected due to the previously explored broadening of close targets for DBS. Otherwise, BP and DBS seem to produce very similar images of targets/features further away when using Hann windowing. Broadening in range and cross range can be harder to spot due to the smoothing action of the window however. The building contour is clearly visible because of the ridges in the copper.

The following Figure 39 demonstrates the response of a car, facing the radar standing on slanted ground as seen in Figure 39(a). The shape of the front of the car is visible in the BP SAR image in 39(b), along with other metallic objects such as the poles and railing. The colour scaling of the image makes it possible to also see the road surface (asphalt)

and the curb to the left.

(a)

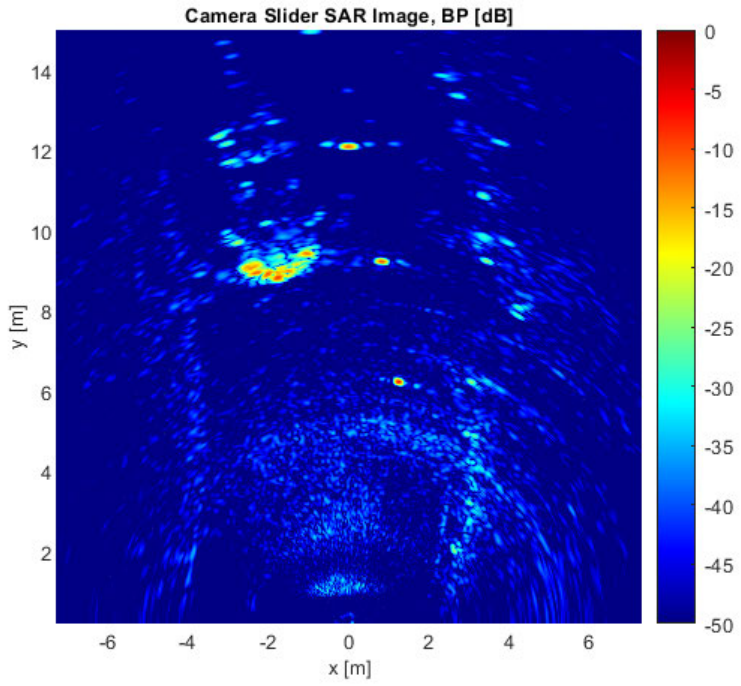

(b)

Figure 39: Camera slider SAR imaging of a car, using the BP algorithm.

To finish off camera slider SAR imaging experiments, we present an image of trees located at the Chalmers campus as shown in Figure 40(a). Amongst the trees was also a bicycle with a steel frame facing the radar sideways. The resulting DBS image is shown in Figure 40(b). A large reflection is noticed in the top right corner of Figure 40(b), which is due to a large metal door not visible in Figure 40(a).

(a)

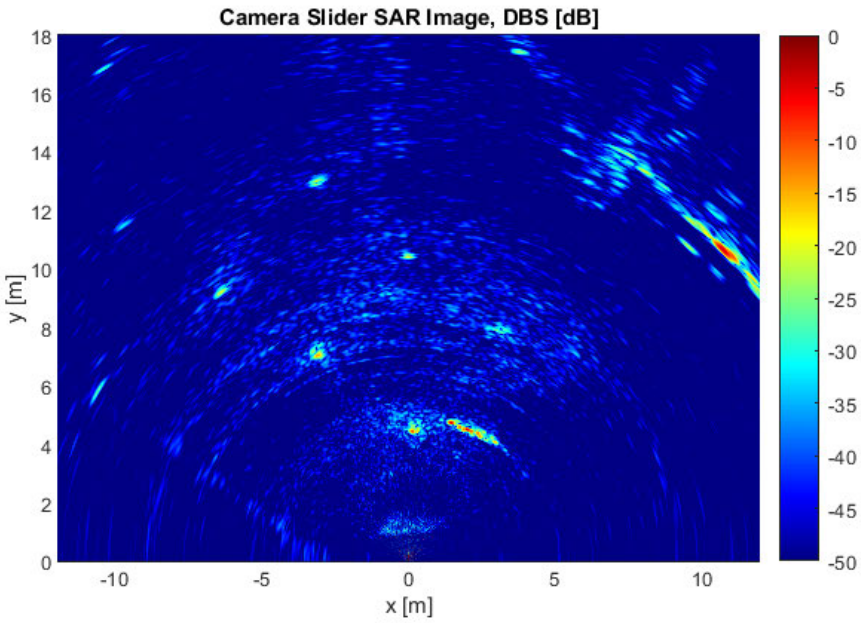

(b)

Figure 40: Imaging of a bicycle facing the radar sideways amongst trees. In (a) the imaging scenario is shown, (b) is the resulting DBS image.

From Figure 40(b), the constellation of trees is clearly visible as well as the extent of the bicycle frame.

4.3.2 Car-mounted SAR

The final imaging experiments, where the radar was mounted in a side-looking position on car, are presented here. In Table 10 and Table 11 the radar parameters used in this section are shown. It should be noted that the parameters were selected so that a fixed range resolution of approximately 6 cm and a cross-range resolution of approximately 5 cm could be obtained at 5 m range at boresight, regardless of the nominal radar speeds being 10 km/h or 30 km/h.

Table 10: Radar parameters, 10 km/h

Parameter	**Value**
f_c	78.5 GHz
f_s	8 MS/s
S	40 MHz/µs
N	512
M	255
T_c	255 µs
B	2.56 GHz
CPI	65 ms
D_{SAR}	$\approx$ 18 cm

Table 11: Radar parameters, 30 km/h

Parameter	**Value**
f_c	78.5 GHz
f_s	8 MS/s
S	40 MHz/µs
N	512
M	255
T_c	85 µs
B	2.56 GHz
CPI	22 ms
D_{SAR}	$\approx$ 18 cm

First, a scene of aluminum foil-clad tubes arranged on the airfield was imaged. The scene and resulting BP images are presented in Figure 41. The SAR images were captured at estimated speeds of 7 km/h and 30 km/h for 41(b) and (c) respectively. Note that scatterers do not end up on the exact same (x, y)-coordinates in images from different sets of data. This is because the measurement setup applied no accurate timing when triggering measurements, which affects the placement of the synthetic aperture center especially in the x-direction.

(a)

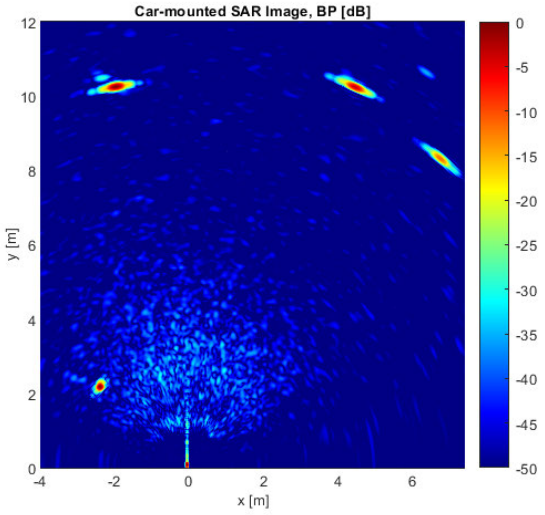

(b)

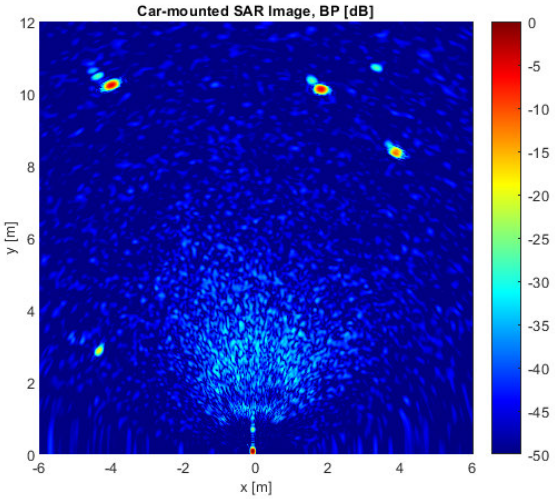

(c)

Figure 41: Scene imaged by a side-looking car mounted radar in (a), and resulting BP SAR images are shown in (b) and (c) for an approximate 10 km/h and 30 km/h driving speed respectively.

Images in Figures 41(b) and (c) succeed in capturing the scene, as placed out targets appear visible and in the correct formation. We can also observe returns from the ground directly in front of the radar. The smaller velocity image seems to experience some broadening in azimuth compared to 30 km/h. This is suspected to be the result of vibrations in the radar platform and was investigated in a further experiment. Next, the road surface was made rougher by laying road marking strips across the car's trajectory as shown in Figure 42.

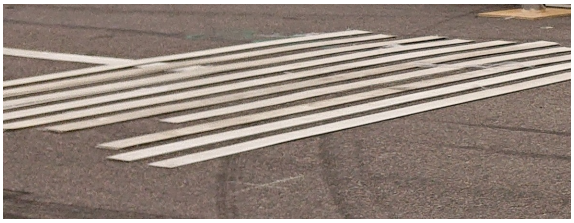

(a)

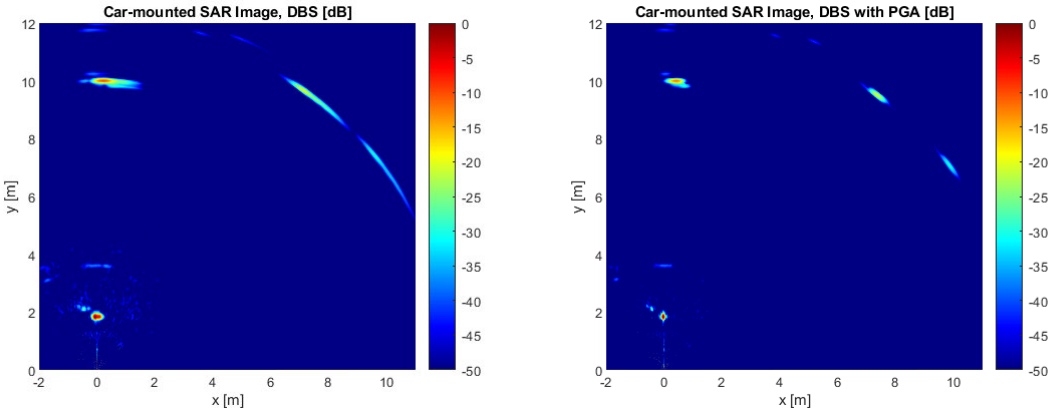

(b) (c)

Figure 42: Road marking strips laid out across the car-trajectory are shown in (a). Resulting DBS SAR images are shown in (b) and (c), where the latter applied the PGA algorithm also.

The resulting DBS image in Figure 42(b) clearly shows that the broadening in cross range is made more significant under rougher road conditions. Specifically, the responses seem smeared and are likely characteristic of phase errors due to low frequency vibrations as explored in simulations (Section 4.2.3). The broadening is shown mendable using the PGA algorithm as shown in Figure 42(c), as the target responses are more focused in the cross-range dimension. It should be noted that the SNR of the right-most targets in the images are worse compared to earlier images presented in Figure 41 of the same scene. This is expected to be partly because of the broadening, but also the relatively large angle from boresight (lower antenna gain) from imperfect triggering of the measurement.

Next, a moving bicyclist was introduced in the scene. The bicyclist was traveling parallel to the car trajectory in the opposite direction (meeting the car) and behind the closest aluminium tube relative to the car. It was agreed before the measurement that the bicyclist would try to achieve a constant speed of around 10 km/h by looking at the installed speedometer, but the actual recorded value might deviate. The resulting BP and DBS images are presented in Figure 43.

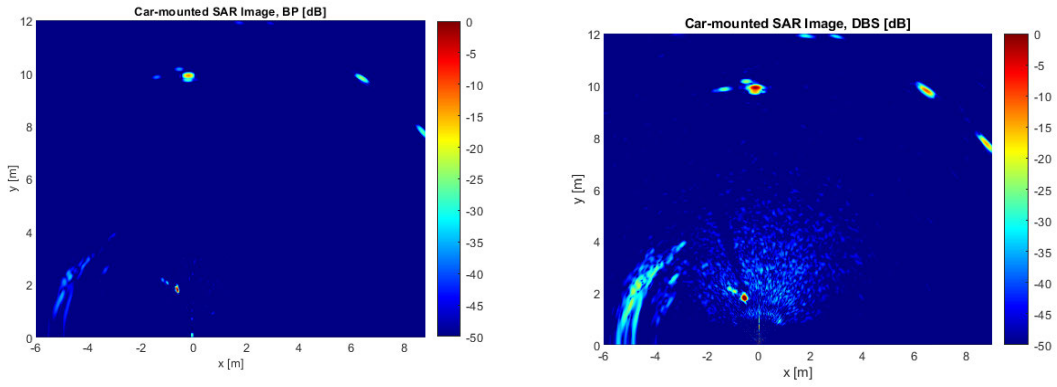

(a) (b)

Figure 43: Resulting BP (a) and DBS (b) SAR images after introducing a moving bicyclist in the scene previously shown in Figure 41(a). The car's speed was estimated to 24 km/h and the bicyclist's is suspected to be roughly 10 km/h but was not measured accurately.

It is evident that the SAR images in Figures 43(a) and (b) cannot capture the bicyclist properly. The response is seen to the bottom left in both images, and appears smeared but also translated in cross range which places the bicyclist almost directly in front of the car. Clearly, moving targets are a challenge for forming SAR images in traffic scenarios. As described by (51) and indirectly explained by Figure 23, angular displacement arises when the ratio between the observed radial velocities and the radar velocity is erroneous. In this case we observe a target that has a radial velocity component towards the radar which means that v_r/v_x is larger than expected meaning that the target gets an angular displacement away from the scene center. Also, when comparing Figures 43(a) and (b), it is apparent that the far away aluminium-clad tubes but also the bicyclist are given less dynamic range compared to DBS. This could potentially be explained by the fact that the close tube-target is better focused for BP, making other targets less significant after normalization compared to the DBS-case.

The target response of a human standing in between two aluminium tubes is shown in Figure 44. All three targets were situated approximately 2.5 m from the car trajectory, and the car moved at a speed of 10 km/h while observing the scene. The human is clearly visible, even though it is standing amongst other metallic scatterers. This image also shows signs of multi-bounce effects, as it contains significant peaks in areas where no actual targets are present in reality. An example of this is the peak at approximately 3.5 m in boresight, directly behind the human. The peak is likely due to the waveform reflecting off one of the tubes first, then propagating to the other tube which scatters the energy back to the radar.

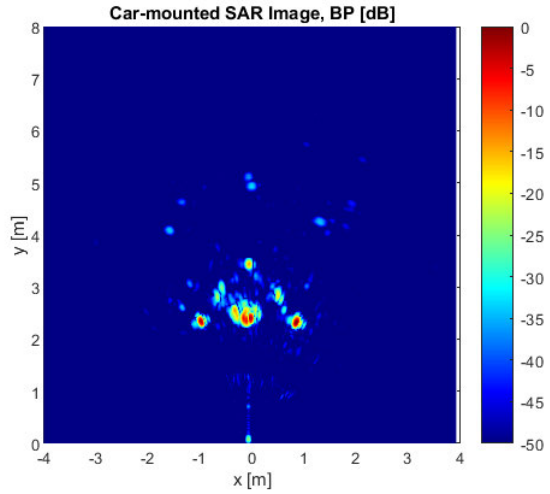

Figure 44: Resulting BP SAR image of a human standing between two aluminium tubes.

Collecting multiple frames as the vehicle moves forward is interesting from an automotive perspective. That means that one can form multiple SAR images that observes the same scene from multiple aperture centers. To study this effect, 4 tubes where placed in the constellation shown in Figure 45(a) where the tubes are divided in pairs which are then placed at the same y-coordinate. The speed of the vehicle was again 10 km/h.

(a)

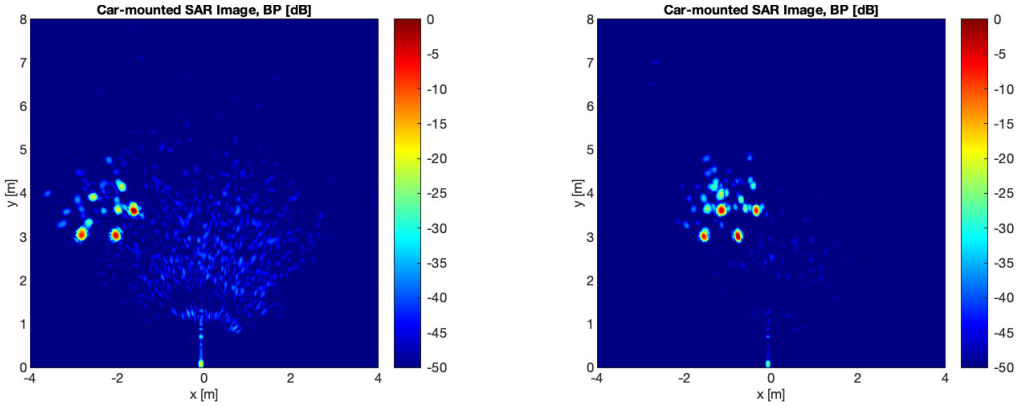

(b) (c)

Figure 45: Scene consisting of 2 sets of tubes on the same y-coordinate (a). The speed of the radar was 10 km/h. Multiple frames where collected and BP-SAR images are shown from frame 1 in (b) and frame 8 in (c) meaning that the vehicle has moved approximately 1.4 m between the measurements.

The result from observing the scene in the first and last collected frame is shown in Figure 45(b) and Figure 45(c). As can be seen, the most apparent effect is that the angle between the aperture center and the tubes changes between the two shots, which makes sense considering that the radar has moved forward approximately 1.4 m. Moreover, in the SAR image from the first frame the upper left tube appears to be completely hidden by the lower right tube in front of it and in the last frame all of the tubes are visible. We can also see indications of multi-bounce effects in the images due to reflections between the tubes.

Another aspect that needs to be considered when SAR images are formed and compared on a frame-to-frame basis is that the radar cross section of real targets might be heavily dependent upon aspect angle. This means that a strong reflection from a target in one frame might be much weaker in the next frame. Further, this might change the appearance of the entire image since we have normalized the intensity in reference to the strongest reflection. An example of a more complicated scene is shown in Figure 46(a) where we have 4 tubes aligned in the direction of motion and a distributed target in the form of a stationary car placed behind them. SAR images was formed on 3 consecutive frames and can be seen in Figure 46(b), 46(c) and 46(d).

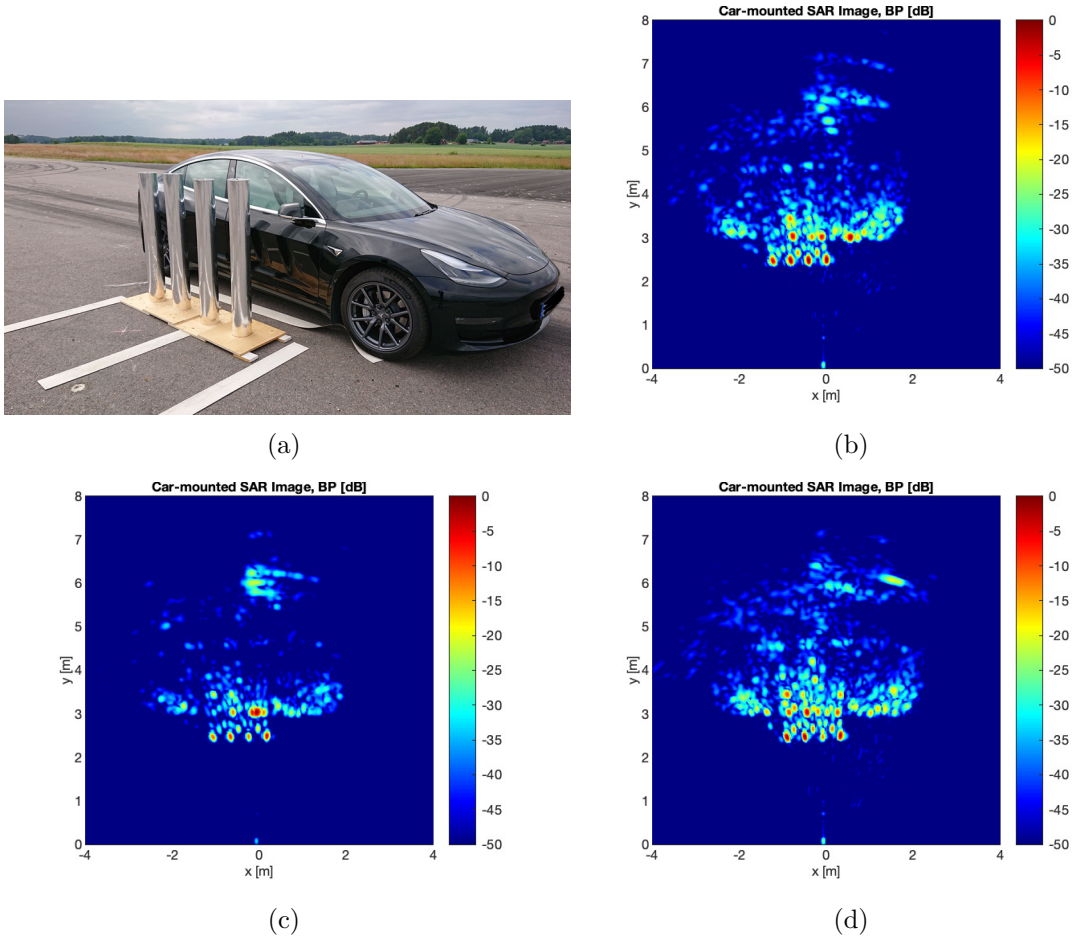

(a) (b) (c) (d)

Figure 46: A more complicated target consisting of 4 poles and a stationary vehicle (a). BP SAR images were formed over 3 consecutive frames. Frame 1(b), Frame 2(c) and Frame 3(d).

As is shown in Figure 46(b) we start off with some clear geometric information about the tubes and the car (particularly its front bumper) but in Figure 46(c), when the radar has moved approximately 18 cm, some of that is lost. Instead we see a very specular reflection somewhere on the front door of the car and in relation to that, the intensity of all other scatters appears to be much weaker. In Figure 46(d), the radar has moved an additional length of approximately 18 cm and most of the geometric information about the car is back. Lastly, it should be noted that we can see a large unexpected reflection behind the car that might be explained by multi-bounce effects. The main conclusion from Figure 45 and 46, however, is that we can collect data using multiple frames which can ultimately be used to produce SAR movies, which is highly interesting for an automotive use-case.

4.4 Summary of Results

In order to finalize the presentation of results produced in this thesis work, a quick summary is made:

- The developed simulation model can generate useful data that mimics what the TI AWR1843 radar outputs. Positional changes of point targets and antenna phase centers are updated on a sample-by-sample basis, i.e., no start-stop approximation is assumed. This data can then be analyzed using conventional FMCW processing methods (including MIMO) as well as with the presented SAR algorithms, namely backprojection and DBS. The measured resolution agrees with theory, meaning considerably finer azimuth resolution than what is possible with eight-channel MIMO.

- DBS rests on a few assumptions such as no range migration and an approximately linear Doppler phase term. Simulation results indicate that range migration can be a problem, but not detrimental for off-boresight targets in scenes of interest for automotive SAR. Similarly, simulation results suggest that the linearity of the Doppler term is questionable for close targets ($\approx 1\,\mathrm{m}$). The effect that can be seen in SAR images when those assumptions are violated images is coarser range and cross-range resolution than in the corresponding images formed with backprojection.

- Vibrations in cars will likely not lead to prominent paired echoes in the formed SAR images with the radar parameters devised in this project. This is particularly interesting from an ADAS perspective where automatic target recognition is used, since SAR image would contain "ghost targets" if paired echoes where present.

- Vibrations will instead likely lead to broadening of main lobes which by definition limits cross range resolution. However, this effect and other spatially invariant phase errors could be suppressed using PGA autofocusing.

- A prototype system with the radar mounted on a motorized camera slider was used to image scenes consisting of point-like targets in the form of trihedral reflectors. SAR images were formed and resolution turned out to agree well with theory. Again, it was shown that the SAR system could produce images with considerably finer azimuth resolution than what was possible with eight-channel MIMO. It was also shown that nearby objects with large differences in RCS could be reliably distinguished from one another.

- The prototype system was also used outside to produce accurate images of more complex scenes consisting of cars, bikes, buildings, asphalt, roadside curbs and trees.

- In the final experiments, the radar was mounted on a real vehicle which proved that the the earlier results were not limited to idealized circumstances and that one could clearly see objects such as cars with very high resolution using automotive SAR. Effects such as estimating radar velocity erroneously, manual triggering and antenna vibrations did affect image quality but all of those problems were shown to be manageable.

- Some imaging effects due to moving targets, shadowing and aspect angle dependent RCS were analyzed and identified as being especially challenging and demands further studies. Lastly, it was shown that the system was capable of producing multiple SAR images of the same scene with data from multiple positions, ultimately resulting in SAR movies, which are highly informative from an automotive perspective.

5 Conclusion

The results of this thesis demonstrates that it is indeed possible to produce high quality SAR images of representative automotive scenarios using the TI-AWR1843 radar in a side-looking mode of operation. This is a very promising result by itself considering that SAR systems are usually operated from aircraft or satellites with ranges and wavelengths being several orders of magnitude larger than the system used in this project. It was shown that a significantly finer resolution in azimuth can be achieved with the same radar system using SAR rather than its MIMO capabilities in the side-looking mode of operation. To reach those conclusions, a mathematical model of the IF signal in FMCW systems was derived and from that model two diametric opposite image formation algorithms; DBS and backprojection were implemented and adapted for an automotive use case.

The DBS algorithm is based on frequency analysis, while backprojection requires a pixel-by-pixel matched filtering approach. In particular, DBS rest on some assumptions that are not always met in automotive scenarios leading to a somewhat coarser resolution than what backprojection was able to produce. However, the processing steps in DBS consists mainly of a 2D-FFT; an operation which is readily available on many automotive radar chipsets.

The derived signal model was also used to develop a simulation model that could successfully reproduce radar data which was useful for testing and evaluating said image formation algorithms, as well as to predict the behaviour of the overall system. Specifically, the phase error that arises due to vibrations in cars was investigated in depth and results indicate that its likely effect is broadening of mainlobes, leading to a coarser cross-range resolution. It was shown that PGA could mitigate that effect and other spatially invariant phase errors. A prototype system using a camera slider proved to be valuable in evaluating system performance in an idealized environment. Lastly the system was implemented on a real vehicle which proved that the system was capable of producing highly informative SAR images in realistic scenarios but also highlighted that further investigation is needed for effects such as dynamic scenes, shadowing and aspect angle dependent RCS.

Appendix

A Discrete time Fourier transform of a complex oscillation

Let n denote discrete time, and Ω' a normalized angular frequency of a complex oscillation

$$s(n) = e^{\,j\Omega' n}.$$

In order to find the DTFT of such a sequence of finite duration with length N, it is convenient to define the Dirichlet kernel $\mathrm{Dir}_N(\Omega)$. This is a function which appears often in digital frequency domain processing, and can be viewed as a periodic equivalent of the sinc-function. It is defined in this thesis as

$$\mathrm{Dir}_N(\Omega) = \frac{\sin(\Omega N/2)}{\sin(\Omega/2)}. \tag{77}$$

The DTFT of $s(n)$ is:

$$\begin{aligned}
\mathrm{DTFT}_n\big\{s(n)\big\} = \sum_{n=-\infty}^{\infty} s(n) e^{\,-j\Omega n} &= \sum_{n=0}^{N-1} e^{\,-j(\Omega\,-\,\Omega')n} \\
&= \frac{1 - e^{\,-j(\Omega\,-\,\Omega')N}}{1 - e^{\,-j(\Omega\,-\,\Omega')}} \\
&= \frac{e^{\,-j(\Omega\,-\,\Omega')N/2}}{e^{\,-j(\Omega\,-\,\Omega')/2}} \cdot \frac{e^{\,j(\Omega\,-\,\Omega')N/2} - e^{\,-j(\Omega\,-\,\Omega')N/2}}{e^{\,j(\Omega\,-\,\Omega')/2} - e^{\,-j(\Omega\,-\,\Omega')/2}} \\
&= e^{\,-j(\Omega\,-\,\Omega')(N\,-\,1)/2} \cdot \frac{\sin\big((\Omega - \Omega')N/2\big)}{\sin\big((\Omega - \Omega')/2\big)} \\
&= e^{\,-j(\Omega\,-\,\Omega')(N\,-\,1)/2} \cdot \mathrm{Dir}_N(\Omega - \Omega')
\end{aligned} \tag{78}$$

written using the Dirichlet kernel. $\mathrm{Dir}_N(\Omega - \Omega')$ is a shift of the function such that the peak is centered at $\Omega = \Omega'$.

For two coupled complex oscillations, as in the case of the IF signal described by (20), the 2D-DTFT can be split in two 1D parts. Let

$$s(n, m) = e^{\,j\Omega' n} e^{\,j\Omega'' m}$$

where the m-dimension is M long. Then, because the 2D-DTFT becomes separable in n and m, we have a multiplication of two 1D-DTFTs:

$$\mathrm{DTFT}_{n,m}\big\{s(n,m)\big\} = \mathrm{DTFT}_n\big\{e^{\,j\Omega' n}\big\} \cdot \mathrm{DTFT}_m\big\{e^{\,j\Omega'' m}\big\} \tag{79}$$

which gives

$$\begin{aligned}
\big|\mathrm{DTFT}_{n,m}\big\{s(n,m)\big\}\big|^2 &= \big|\mathrm{Dir}_N(\Omega - \Omega') \cdot \mathrm{Dir}_M(\Omega - \Omega'')\big|^2 \\
&= \left|\frac{\sin\big((\Omega - \Omega')N/2\big)}{\sin\big((\Omega - \Omega')/2\big)} \cdot \frac{\sin\big((\Omega - \Omega'')M/2\big)}{\sin\big((\Omega - \Omega'')/2\big)}\right|^2
\end{aligned} \tag{80}$$

where the multiplicative phases in the last expression of (78) are left out since they are of magnitude one.

B Mathematics behind backprojection in FMCW radars

With the start-stop approximation $\tau_{n,m} = \tau_m$, the IF-signal model can be written as

$$\begin{aligned} s_{\text{if}}(n,m) &= \frac{\alpha}{2} e^{\,j2\pi S\tau_m(nT_s - T/2) + 2\pi f_c\tau_m - \pi S\tau_m^2} \\ &= \frac{\alpha}{2} e^{\,j\Omega_{\text{fast}}n} \cdot e^{\,j(2\pi f_c\tau_m - \pi ST\tau_m - \pi S\tau_m^2)} \end{aligned} \tag{81}$$

where $\Omega_{\text{fast}} = 2\pi ST_s\tau_m$. The DTFT in fast-time domain only of this 2D signal is then

$$\begin{aligned} S(\Omega_R, m) &= \text{DTFT}_n\big\{s_{\text{if}}(n,m)\big\} = \sum_{n=-\infty}^{\infty} s_{\text{if}}(n,m) e^{\,-j\Omega_R n} \\ &= \frac{\alpha}{2} \sum_{n=0}^{N-1} e^{\,-j(\Omega_R - \Omega_{\text{fast}})n} \cdot e^{\,j(2\pi f_c\tau_m - \pi ST\tau_m - \pi S\tau_m^2)} \\ &= \frac{\alpha}{2} e^{\,-j(\Omega_R - \Omega_{\text{fast}})(N-1)/2} \cdot \text{Dir}_N(\Omega_R - \Omega_{\text{fast}}) \cdot e^{\,j(2\pi f_c\tau_m - \pi ST\tau_m - \pi S\tau_m^2)} \\ &= \frac{\alpha}{2} e^{\,-j(\Omega_R(N-1)/2} \cdot \text{Dir}_N(\Omega_R - \Omega_{\text{fast}}) \cdot e^{\,j(2\pi f_c\tau_m - \pi ST\tau_m - \pi S\tau_m^2)} \cdot e^{\,j\Omega_{\text{fast}}(N-1)/2} \\ &= \frac{\alpha}{2} e^{\,-j\Omega_R(N-1)/2} \cdot \text{Dir}_N(\Omega_R - \Omega_{\text{fast}}) \cdot e^{\,j(2\pi f_c\tau_m - \pi ST_s\tau_m - \pi S\tau_m^2)} \end{aligned} \tag{82}$$

where we have used (77) in the second step and utilized that $\Omega_{\text{fast}}(N-1)/2 = \pi ST\tau_m - \pi ST_s\tau_m$ in the last step. Image formation using backprojection includes matched filtering in slow time with coherent range compressed signals [21]. In order to do that with the FMCW digitized data, we need to cancel out the range dependant phase term in (82). The frequency domain filter that does this can be expressed as

$$H_R(\Omega_R, m) = e^{\,j\Omega_R(N-1)/2} \tag{83}$$

where it should be mentioned that when this filter was implemented, the actual sign for the phase term in this expression depended on whether the generated data was generated artificially in simulations or was outputted from the TI AWR1843 radar. With the sign convention derived here, the coherent range compressed signals can be written as

$$\begin{aligned} S_f(\Omega_R, m) &= S(\Omega_R, m) H_R(\Omega_R, m) \\ &= \frac{\alpha}{2} \text{Dir}_N(\Omega_R - \Omega_{\text{fast}}) \cdot e^{\,j(2\pi f_c\tau_m - \pi ST_s\tau_m - \pi S\tau_m^2)}. \end{aligned} \tag{84}$$

To form an image we need to relate the coherent range profiles to a particular geometry in the form of pixel coordinates as in Figure 12. Assuming we know the antenna positions at all slow times samples m, we can compute the one way distance between all pixel coordinates (x_k, y_k) and the antennas over slow time as

$$R_{m,k} = \sqrt{y_k^2 + (x_k - a_m)^2} \tag{85}$$

where a_m is the antenna x-coordinate. The corresponding delay and normalized angular frequency is given by

$$\tau_{m,k} = \frac{2R_{m,k}}{c} \tag{86}$$

$$\Omega_{m,k} = 2\pi S T_s \tau_{m,k}. \tag{87}$$

The idea with backprojection is to iterate through all pixel coordinates one after another and consider a hypothetical unit reflector ($\alpha/2 = 1$) for each of them. Based on the derived model, we can then create a signal that has the same phase evolution in slow time as experienced by one such unit reflector when the radar moves. The conjugate of this signal defined locally for each pixel will be the slow-time matched filter

$$H_D(\tau_{m,k}) = e^{j(-2\pi f_c \tau_{m,k} + \pi S T_s \tau_{m,k} + \pi S \tau_{m,k}^2)}. \tag{88}$$

It should also be noted that in some papers that treats backprojection for FMCW radars such as [18], [13] and [9], the only phase term that is removed is the Doppler term, meaning that (88) is approximated as a Doppler term and a phase constant

$$H_D(\tau_{m,k}) \approx e^{-j2\pi f_c \tau_{m,k}} \cdot e^{j\varphi_k}. \tag{89}$$

The validity of this assumption for the chirp parameters used in automotive SAR is discussed in Section 2.5.2. One obstacle remains in practice and it is to interpolate (84) so Ω_R is well defined at $\tau_{m,k}$. The method used in this project is linear interpolation and we will call the interpolated frequency variable $\Omega_{m,k}$. The intensity image is obtained by simply filtering the interpolated coherent range compressed signal through a filter matched to each pixel as shown in Figure 13. The final expression is

$$I_k = \left| \sum_{m=0}^{M-1} S_f(\Omega_{m,k}, m) \cdot e^{-j2\pi f_c \tau_{m,k}} \cdot e^{j\varphi_k} \right|^2 = \frac{\alpha^2}{4} \left| \sum_{m=0}^{M-1} \mathrm{Dir}_N(\Omega_{m,k} - \Omega_{\text{fast}}) \right|^2. \tag{90}$$

References

[1] S. M. Patole, M. Torlak, D. Wang, and M. Ali. "Automotive radars: A review of signal processing techniques". In: *IEEE Signal Processing Magazine* vol. 34 (Mar. 2017), pp. 22–35. DOI: 10.1109/MSP.2016.2628914.

[2] J. Hasch. "Driving towards 2020: Automotive radar technology trends". In: *2015 IEEE MTT-S International Conference on Microwaves for Intelligent Mobility (ICMIM)*. Heidelberg, Germany, Apr. 2015, pp. 1–4. DOI: 10.1109/ICMIM.2015.7117956.

[3] C. Iovescu and S. Rao. *The fundamentals of millimeter wave sensors*. White Paper. Texas Instruments. Dallas TX, United States of America, July 2020. URL: https://www.ti.com/sensors/mmwave-radar/what-is-mmwave.html.

[4] Veoneer Inc. *Radar*. 2021. URL: https://www.veoneer.com/en/radar.

[5] C. Wiley. "Synthetic Aperture Radars : A Paradigm for Technology Evolution". In: *IEEE Transactions on Aerospace and Electronic Systems* vol. 21-3 (1985), pp. 440–443. DOI: 10.1109/TAES.1985.310578. URL: https://ci.nii.ac.jp/naid/30026095323/en/.

[6] M. Soumekh. "INTRODUCTION". In: *Synthetic Aperture Radar Signal Processing with MATLAB Algorithms*. New York N.Y, USA: John Wiley & Sons, inc., 1999.

[7] J. C. Curlander and R. N. McDonough. "INTRODUCTION TO SAR". In: *Synthetic Aperture Radar - Systems And Signal Processing*. John Wiley & Sons, Inc., 1991. Chap. 1.

[8] R. J. Sullivan. "Introduction to SAR". In: *Radar Foundations for Imaging and Advanced Concepts*. Raleigh NC, USA: SciTech Publishing Inc., 2004. Chap. 7.1.

[9] F. Harrer, F. Pfeiffer, A. Löffler, T. Gisder, and E. Biebl. "Synthetic aperture radar algorithm for a global amplitude map". In: *2017 14th Workshop on Positioning, Navigation and Communications (WPNC)*. Bremen, Germany, Oct. 2017, pp. 1–6. DOI: 10.1109/WPNC.2017.8250080.

[10] A. Laribi, M. Hahn, J. Dickmann, and C. Waldschmidt. "Performance Investigation of Automotive SAR Imaging". In: *2018 IEEE MTT-S International Conference on Microwaves for Intelligent Mobility (ICMIM)*. Munich, Germany, Apr. 2018, pp. 1–4. DOI: 10.1109/ICMIM.2018.8443554.

[11] L. Daniel, A. Stove, E. Hoare, et al. "Application of Doppler beam sharpening for azimuth refinement in prospective low-THz automotive radars". In: *IET Radar, Sonar & Navigation* vol. 12 (Aug. 2018), pp. 1121–1130. URL: https://digital-library.theiet.org/content/journals/10.1049/iet-rsn.2018.5024.

[12] T. Kan, G. Xin, L. Xiaowei, and L. Zhongshan. "Implementation of Real-time Automotive SAR Imaging". In: *2020 IEEE 11th Sensor Array and Multichannel Signal Processing Workshop (SAM)*. Hangzhou, China, June 2020, pp. 1–4. DOI: 10.1109/SAM48682.2020.9104293.

[13] X. Gao, S. Roy, and G. Xing. "MIMO-SAR: A Hierarchical High-Resolution Imaging Algorithm for mmWave FMCW Radar in Autonomous Driving". In: *IEEE Transactions on Vehicular Technology* vol. 70 (Aug. 2021), pp. 7322–7334. DOI: 10.1109/TVT.2021.3092355.

[14] B. M. Keel and J. M. Baden. “STRETCH PROCESSING”. In: *Principles of Modern Radar Volume 2: Advanced Techniques*. Raleigh NC, USA: SciTech Publishing Inc., 2013. Chap. 2.2.4-2.2.4.2.

[15] V. Dham. *Programming Chirp Parameters in TI Radar Devices*. Application Report. Texas Instruments. Dallas TX, United States of America, Feb. 2020. URL: https://www.ti.com/lit/an/swra553a/swra553a.pdf?ts=1628143440604.

[16] R. J. Sullivan. “SAR Waveforms and Processing”. In: *Radar Foundations for Imaging and Advanced Concepts*. Raleigh NC, USA: SciTech Publishing Inc., 2004. Chap. 7.2.

[17] M. A. Richards. “Digital Signal Processing Fundamentals for Radar”. In: *Principles of Modern Radar : Basic Principles, Volume 1*. Raleigh NC, USA: SciTech Publishing Inc., 2010. Chap. 14.

[18] A. Ribalta. “Time-Domain Reconstruction Algorithms for FMCW-SAR”. In: *IEEE Geoscience and Remote Sensing Letters* vol. 8 (May 2011), pp. 396–400. DOI: 10.1109/LGRS.2010.2078486.

[19] W. G. Carrara, R. S. Goodman, and Majewski R. M. “Appendix D: Sidelobe Control in SAR Imagery”. In: *Spotlight Synthetic Aperture Radar Signal Processing Algorithms*. Norwood MA, USA: Artech House, 1995.

[20] S. Rao. *MIMO Radar*. Application Report. Texas Instruments. Dallas TX, United States of America, July 2018. URL: https://www.ti.com/lit/an/swra554a/swra554a.pdf?ts=1633893699334.

[21] M. Soumekh. “Generic Synthetic Aperture Radar”. In: *Synthetic Aperture Radar Signal Processing with MATLAB Algorithms*. New York N.Y, USA: John Wiley & Sons, inc., 1999. Chap. 4.

[22] W. G. Carrara, R. S. Goodman, and Majewski R. M. “Phase Errors”. In: *Spotlight Synthetic Aperture Radar Signal Processing Algorithms*. Norwood MA, USA: Artech House, 1995. Chap. 6.

[23] W. G. Carrara, R. S. Goodman, and Majewski R. M. “Autofocus Techniques”. In: *Spotlight Synthetic Aperture Radar Signal Processing Algorithms*. Norwood MA, USA: Artech House, 1995. Chap. 6.

[24] D. E. Wahl, P. H. Eichel, D. C. Ghiglia, and C. V. Jakowatz. “Phase gradient autofocus - a robust tool for high resolution SAR phase correction”. In: *IEEE Transactions on Aerospace and Electronic Systems* vol. 30 (July 1994), pp. 827–835. DOI: 10.1109/7.303752.

[25] R. J. Sullivan. “Radar Cross-Section”. In: *Radar Foundations for Imaging and Advanced Concepts*. Raleigh NC, USA: SciTech Publishing Inc., 2004. Chap. 3.1.

[26] R. J. Sullivan. “Reception of Scattered Energy”. In: *Radar Foundations for Imaging and Advanced Concepts*. Raleigh NC, USA: SciTech Publishing Inc., 2004. Chap. 1.8.

[27] P. Kildal. “Transmission line model for rectangular patch”. In: *Foundations of Antenna Engineering: A Unified Approach for Line-of-Sight and Multipath*. Gothenburg, Sweden: Kildal Antenn AB, 2015. Chap. 6.1.

[28] Texas Instruments. *xWR1843 Evaluation Module (xWR1843BOOST) Single-Chip mmWave Sensing Solution*. Users’ Guide. Dallas TX, United States of America, 2020. URL: https://www.ti.com/lit/ug/spruim4b/spruim4b.pdf?ts=1631600762908.